

Article

Investigating the Role of Gravity Waves on Equatorial Ionospheric Irregularities Using TIMED/SABER and C/NOFS Satellite Observations

Melessew Nigussie ^{1,*} , Mark Moldwin ^{2,*} and Endawoke Yizengaw ^{3,*}

¹ Washera Geospace and Radar Science Research Laboratory, Physics Department, Science College, Bahir Dar University, Bahir Dar P.O. Box 79, Ethiopia

² Department of Climate and Space Sciences and Engineering, University of Michigan, Ann Arbor, MI 48108, USA

³ Space Science Application Laboratory, The Aerospace Corporation, El Segundo, CA 90245, USA

* Correspondence: melessewnigussie@yahoo.com (M.N.); mmoldwin@umich.edu (M.M.); endawoke.yizengaw@aero.org (E.Y.)

Abstract: In this paper, for the first time, simultaneous atmospheric temperature perturbation profiles obtained from the TIMED/SABER satellite and equatorial ion density and vertical plasma drift velocity observations with and without ESF activity obtained from the C/NOFS satellite are used to investigate the effect of gravity waves (GW) on ESF. The horizontal and vertical wavelengths of ionospheric oscillations and GWs are estimated by applying wavelet analysis techniques. In addition, vertically propagating GWs that dissipate energy in the ionosphere-thermosphere system are investigated using the spectral analysis technique. We find that the vertical wavelength of GW, corresponding to dominant wavelet power, ranges from 12 to 31 km regardless of the conditions of the ionosphere; however, GWs with vertical wavelengths between about 1 to 13 km are found every day, saturated between 90 and 110 km at different longitudinal sectors. Filtering out vertical wavelengths above 13 km from temperature perturbations, ranges of zonal wavelengths of GW (i.e., from about 290 to 950 km) are found corresponding to irregular and non-irregular ionosphere. Similarly, corresponding to dominant oscillations, the zonal wavelength of ion density perturbations is found within 16 to 1520 km. Moreover, we find an excellent agreement among the median zonal wavelengths of GW for the cases of irregular and non-irregular ionosphere and ion density perturbations that are 518, 495, and 491 km, respectively. The results imply that seed perturbations due to GW with a vertical wavelength from about 1 to 13 km evolve to ion density irregularity and may be amplified due to post-sunset vertical upward drift velocity.



Citation: Nigussie, M.; Moldwin, M.; Yizengaw, E. Investigating the Role of Gravity Waves on Equatorial Ionospheric Irregularities Using TIMED/SABER and C/NOFS Satellite Observations. *Atmosphere* **2022**, *13*, 1414. <https://doi.org/10.3390/atmos13091414>

Academic Editor: Masashi Hayakawa

Received: 1 August 2022

Accepted: 26 August 2022

Published: 1 September 2022

Publisher's Note: MDPI stays neutral with regard to jurisdictional claims in published maps and institutional affiliations.



Copyright: © 2022 by the authors. Licensee MDPI, Basel, Switzerland. This article is an open access article distributed under the terms and conditions of the Creative Commons Attribution (CC BY) license (<https://creativecommons.org/licenses/by/4.0/>).

Keywords: gravity wave; equatorial spread F; C/NOFS satellite; SABER satellite

1. Background of the Study

The Equatorial ionosphere exhibits very dynamic behavior, for instance, equatorial spread F (ESF), mainly in the evening sector [1]. ESF is the generic name given to the evening time equatorial ionospheric irregularity. The zonal electric field (or $E \times B$) which usually gets enhanced in the evening time uplifts the ionosphere [2]. In the meantime, the ionization at the lower altitude of the bottom side F-layer decays faster than the upper part due to high recombination with neutrals and the disappearance of photoionization. This implies that a high vertical ionization density gradient below the F-layer peak can be created. This sets up the condition of highly dense plasma above the less dense plasma which creates a conducive situation for instability of the ionosphere. This means the bottom side evening time equatorial ionosphere can be easily perturbed, for example, due to locally generated polarized electric field as a result of gravity-driven current. The growth of the instabilities created at the bottom side can be affected by the neutral wind speed [3].

Observational studies show that perturbations formed at the bottom side of the F-layer can grow upward and appear in the form of electron density depletions usually called plasma bubbles. It is recognized that ESF is likely described by the gravity-driven Rayleigh-Taylor Instability (RTI) [1,4–7]. The growth rate of the generalized Rayleigh-Taylor instability is given by [7]

$$\gamma_{RT} = \frac{\Sigma^F}{\Sigma^E + \Sigma^F} \frac{\partial N}{N \partial h} \left(\frac{E}{B} - \frac{g}{\nu} + U_n \right) - R \quad (1)$$

where Σ^E and Σ^F are field-aligned integrated E and F region Pederson conductivities, respectively, N is field-aligned integrated electron density, $\frac{\partial N}{\partial h}$ is the vertical electron density gradient, $\frac{E}{B}$ is the plasma vertical drift velocity, g is the gravitational acceleration, ν is collision frequency, U_n is the vertical neutral wind speed, and R is field-aligned integrated recombination rate between the neutral and ionized particles of the Earth's atmosphere.

Since the discovery of ESF, significant efforts have been made to understand its generation and growth mechanisms using experimental and modeling approaches [5,7–11]. Analysis of radar, ionosonde, and Low Earth Orbiting (LEO) satellite data indicate that the generation mechanism of the irregularity is mainly controlled by plasma vertical drift velocity ($E \times B$) [8,9,12–15]. In some of these works [9,13] a threshold altitude has been suggested where the bottom part of the F-layer should be above before the generation of the perturbation occurs. Refs. [8,9,14] have also indicated that drift velocity is the necessary, but not sufficient, condition for the generation of the perturbation; the density gradient could also have a significant effect on the generation of perturbations. However, [13] have shown that the contribution of the density gradient at the bottom side of the F-layer has less significance compared to the height of the F-layer (or drift velocity).

Different numerical techniques have also been developed and implemented to understand the RTI growth and suppression rates [11,16]. The meridional/trans-equatorial wind suppresses the growth of ESF [17–19]; whereas, the vertical and zonal neutral winds enhance the growth of the ESF [7]. On the other hand, [20,21] have indicated that the meridional wind enhances the growth rate of the RTI. Ref. [3] have performed plasma fluid-type numerical simulations and showed that the collisional RTI causes linear growth in the bottom side F-layer and evolves non-linearly as plasma density depletes and moves to higher altitudes due to $E \times B$ drift. Ref. [7] also computed RTI growth rate using basic input parameters such as neutral wind speed, zonal electric field, ionospheric density gradient, and recombination rate and found good agreement between climatological RTI growth rates and monthly and yearly occurrence of ESF; however, the day-to-day prediction is still a challenging problem. In addition, the solar terminator geomagnetic field-aligned hypothesis [22] is a well-accepted idea in describing the climatological behavior of ESF; but not enough in describing the day-to-day variability of ESF [18,23]. Consequently, it is suggested the existence of seed perturbation, for instance, is due to atmospheric gravity waves for the occurrence of ESF [7,24,25]. In situ generation of gravity waves on the ionosphere-thermosphere system can be generated due to different mechanisms such as convection, orographical features, jet streams, and earthquakes among others [26]. Once generated, they can propagate vertically and horizontally and affect the distribution of ionization density in the ionosphere [27].

The effect of gravity waves on ionization density variability has been investigated by analyzing modeled and experimental ionospheric parameters. Usually, the scale size of the zonal structure between the adjacent plasma bubbles is considered as the horizontal wavelength of ionospheric irregularity. Different scales of oscillation of the equatorial ionospheric irregularities have been identified by different researchers. Ref. [28], by carrying out short wave oblique incidence measurements, found a 380 km median horizontal wavelength of the plasma bubbles. Ref. [29], using ROCSAT-1 and IMAGE satellites observations, estimated a 300–1000 km separation distance between plasma bubbles and they argued that this horizontal structure is the manifestation of the atmospheric gravity waves. Similarly, [30] determined a 370–1000 km separation distance between plasma bubbles using atmospheric radar in the Indonesia sector and they speculated that this

horizontal structure of the plasma is generated by atmospheric gravity waves that have similar horizontal wavelengths. Moreover, [31], using AE-E satellite data, identified classes of horizontal structure of plasma bubbles and they concluded that gravity waves with horizontal wavelengths about 1000 km dominantly seed the African sector ionospheric irregularity, whereas about 100 km scale size gravity waves seed both African and Pacific sectors. Ref. [32] also identified, using ALTAIR incoherent scatter radar data, 400 km wavelength of large-scale longitudinal structure of the atmospheric gravity waves. The above investigations and others [24,33–35] suggested that atmospheric gravity waves can be the seeding mechanism of equatorial ionospheric irregularities. Investigations of the correlation between zonal oscillation characteristics of the gravity waves coming from the lower atmosphere and ionospheric irregularities have not yet been done using simultaneous gravity wave and ionospheric observations.

LEO satellite missions are being widely used to monitor the dynamics and electro-dynamics of the lower and upper (ionosphere) atmosphere of the Earth. The Communication/Navigation Outage Forecast System (C/NOFS) satellite was developed by the American Air Force Research Laboratory Space Vehicles Directorate in order to understand, model and forecast the Earth's equatorial ionospheric irregularities [36]. Similarly, NASA's Thermosphere-Ionosphere-Mesosphere Energetic and Dynamics (TIMED) satellite is dedicated to understanding the dynamics and chemistry of Mesosphere-Lower-Thermosphere, (MLT) [37]. Temperature profiles, from the Earth's surface to about 110 km altitude, from the TIMED satellite, are an excellent resource to investigate different parameters of gravity waves [38]. For example, it is useful to determine the potential energy of gravity waves as a function of altitude. The amount of initial perturbation of ionization due to gravity waves is strongly dependent on the amount of energy transferred from gravity waves. In addition, the instabilities/turbulence during gravity wave deposition, if it is done at ionospheric heights, can directly affect the bulk flow speed of the neutral atmosphere, which in turn modulates other ionospheric parameters such as the growth rate of the RTI, zonal electric field, and height of the ionosphere that are usually used for ESF occurrence investigation. This indicates that a combination of TIMED and C/NOFS observations could provide an unprecedented opportunity to investigate the ranges of atmospheric gravity waves that transfers momentum and energy to the neutral atmosphere at ionospheric height. Particularly, temperature profiles from TIMED combined with C/NOFS ionospheric observations will be useful to answer the following questions: which range of gravity waves dissipate the energy responsible for the formation of ESF? At what altitude do gravity waves transfer energy to the ionosphere-thermosphere system? Do gravity waves always transfer energy to the ionosphere-thermosphere system? Are zonal oscillation characteristics of gravity waves from MLT and ESF irregularity similar?

The purpose of this study is to look for answers to the questions raised above. Usually, the characteristics of gravity waves have been inferred from ionospheric observations and models. Fortunately, the fluctuation of atmospheric temperature profiles that can be obtained from the TIMED satellite can be considered as gravity wave observations from which many gravity wave characteristics can be derived. Therefore, the goal of this study is to investigate the scale sizes of gravity waves that dissipate energy and momentum to lower ionosphere-thermosphere systems and are responsible for seeding the ESF. This has been done by analyzing atmospheric temperature profiles between the surface of the Earth to about 110 km altitude obtained from TIMED observations, and ion density and vertical drift velocity observations with and without ESF activity from Ion Velocity Meter (IVM) on C/NOFS. Analysis techniques used for this study, results, discussion, and conclusions are provided in Section 2, Section 3, Section 4, and Section 5, respectively.

2. Data and Analysis Method

2.1. Data

In this study, equatorial atmospheric and ionospheric data obtained from two LEO satellites have been used. C/NOFS satellite was developed by the American Air Force

Research Laboratory Space Vehicles Directorate in order to understand, model, and forecast the Earth's equatorial ionospheric irregularities [36]. C/NOFS was launched in 2008 (decommissioned in early 2015) and had an elliptical orbit at altitudes from 375 to 850 km, with orbital periods of 96 min and an inclination of 13° . The instruments onboard C/NOFS include the Planar Langmuir Probe (PLP) and Ion Velocity Meter (IVM) which were dedicated to measuring the ion density and velocity, respectively [36]. C/NOFS data are publicly available. The one-second average sampling distance between C/NOFS observations is about 6.7 km. This spatial sampling interval is used for wavelet analysis of the C/NOFS data. When both C/NOFS and TIMED/SABER satellites monitor similar regions of the Earth's atmosphere, ion density and plasma vertical drift velocity measurements with and without equatorial spread F activity are taken to study the characteristics of the equatorial ionosphere. As a case study limited in situ ion density and drift velocity measurements are considered in October 2011. Similarly, MLT temperature profiles, obtained from NASA's satellite Thermosphere-Ionosphere-Mesosphere Energetic and Dynamics (TIMED) within C/NOFS observation space and time ranges, have been used for investigating the role of gravity waves on equatorial ionospheric irregularity. TIMED was launched on 7 December 2001 and is functioning to date to help understand the dynamics and chemistry of the MLT [37]. It is orbiting the Earth with an orbital altitude of about 625 ± 25 km and an inclination of $74 \pm 1^\circ$. Sounding of Atmosphere using Broadband Emission Radiometry (SABER) is one of the four instruments onboard the TIMED satellite. SABER is the multi-channel infrared radiometer developed to measure emissions by atmospheric gases in a wide altitude range. The MLT temperature profiles (vertical resolution of 2.2 km) have been retrieved from measurements of CO_2 emissions (~ 1.7 to $17 \mu\text{m}$) by applying the non-local thermodynamic equilibrium inversion techniques [39]. Ref. [40] have compared TIMED temperature profiles (between 30 and 110 km altitude) with independent Rayleigh Lidar measurements and found good agreement indicating the reliability of TIMED data for atmospheric studies. In this study version 2 label, 2A temperature profiles obtained from TIMED have been used. Temperature profiles obtained within geographic latitudes ranging from -20 to 20° , during the presence and absence of ESF activity in the post-sunset sector, have been used in the analysis. In addition, to investigate the day-to-day activity of gravity waves, temperature profiles obtained in the year 2013 (solar maximum, yearly mean, minimum, and maximum F10.7 values are 123, 92, and 174 sfu, respectively) between 17:00 and 19:30 LT and -20 and 20° of latitude have also been used. Of this one year of data, five months (April, June, August, October, and December) of data are selected based on the above criteria. To be more specific the numbers of days of data for these months respectively are 15, 12, 13, 12, and 13; three additional days in October 2011 have been analyzed.

2.2. Analysis Methods

2.2.1. Estimation of Characteristics of Vertically Propagating Gravity Wave

The atmospheric temperature profile is believed to be composed of the background and fluctuating temperature profiles due to different oscillation mode waves such as gravity waves. Identifying the characteristics of gravity waves from the temperature profiles requires removing the background temperature profile. Least square fitting with different order polynomials has been usually applied to estimate the background temperature profiles [41,42]. Ref. [42] tested the importance of using different polynomials such as linear, second, third, and fourth order, and also a low pass filter to estimate the background temperature and found no substantial difference, hence, they used a second order polynomial for their work. Refs. [43,44] proposed to use a high pass filter, with 10 and 15 km cut-off wavelengths, respectively claiming that vertically propagating gravity waves can be contaminated by long wavelength waves (such as tides and planetary). On the contrary, [45] argued that the contamination due to tides and planetary waves is very limited and so no filtering technique needs to be applied. Many also agree that separating gravity waves from other oscillation modes cannot be done perfectly and they considered it a challenging task [42,46,47]. In the present study, the background temperature profile and ion density

variations are estimated by fitting a second order polynomial as was done by [42], and hence the temperature profiles and ion density perturbations are estimated by subtracting the background quantity from the original measurements.

There is no clear-cut boundary for the vertical wavelength of gravity waves [46,48–50]. For example, [46] have determined gravity waves with vertical wavelengths from 2 to 10 km and 2 to 20 km using both wind and temperature measurements. Similarly, [49,50] have obtained vertical wavelengths ranging from 2 to 10 km and 5 to 15 km, respectively. Moreover, [48] and the references therein determined vertical gravity waves with wavelengths from 5 to 25 km and 6 to 30 km from two different data sources. In the present study, after getting background temperature profiles (T_o), fitting the second-order polynomial, temperature perturbation ($T_p = T - T_o$) profiles are estimated. Vertically propagating gravity wave amplitude is believed to be reflected in the normalized temperature fluctuations (T_p/T_o). This temperature fluctuation is extensively used to estimate different gravity wave parameters such as energy and momentum transfer from the wave to the atmosphere, spectral density, and vertical and horizontal wavelengths of gravity waves [38,51,52]. Ref. [38] and the references therein have expressed the potential energy of the gravity wave as a function of altitude, z by

$$E_p(z) = \frac{1}{2} \left(\frac{g(z)}{N(z)} \right)^2 \left(\frac{T_p(z)}{T_o(z)} \right)^2 \quad (2)$$

where $g(z)$ is the acceleration due to gravity. $N(z)$ is the oscillation frequency of the parcel of the atmosphere (usually called Buoyancy or Brunt-Väisälä frequency) and it is expressed as

$$N^2(z) = \frac{g(z)}{T_o(z)} \left(\frac{\partial T_o(z)}{\partial z} + \Gamma_d \right) \quad (3)$$

where $\Gamma_d = g/c_p$ is adiabatic laps rate, c_p is the specific heat capacity of the atmosphere and for this study, 9.8×10^{-3} (K/m) laps rate is adopted. It is well known that the amplitude of gravity waves increases exponentially when they move from low to upper atmosphere as a consequence of decreasing atmospheric density with increasing height [53,54]. At some point at high altitude (critical height), the amplitude of fluctuation of the gravity wave reaches maximum. Consequently, the wave breaks above this height and induces instability or convection [55], which in turn alters the dynamics and electrodynamics of the lower thermosphere. The breaking of the gravity wave is described by different characteristics such as ceasing the growth of the amplitude of fluctuation (or saturation) due to the extraction of energy from the wave to the atmosphere [55] and decreasing the potential energy above this height. The saturation of vertically propagating gravity waves is well described by the linear gravity wave saturation theory [55,56]. From gravity wave linear saturation theory [54,56] and the references therein, gravity wave saturated power spectral density (PSD), for temperature perturbation is given by

$$F_T^s(k_v) \approx \frac{1}{10} \left(\frac{N^4}{g^2 k_v^3} \right) \quad (4)$$

where $k_v (= 2\pi/\lambda_v)$ and λ_v are vertical wave number and wavelength, respectively. The effectiveness of this theory has been tested by comparing the PSD of gravity waves from experimental data with the PSD from equation (4) and found excellent agreement [56–58]. Ref. [59] devised the best way to estimate PSD from atmospheric parameter observations and identified artifacts involved in the traditional approaches used by [57,58]. This robust method is applied in this study to estimate the PSD of gravity waves from normalized temperature fluctuation obtained from the TIMED satellite. The method details are described in [59]. The range of gravity waves that transfer energy and momentum to the lower ionosphere-thermosphere system and the altitude where those waves dissipate energy is investigated by comparing the empirical and theoretical PSD. First by identifying the range of wavelengths of gravity waves that dissipate energy above 90 km in the ionosphere-

thermosphere using this method, horizontal oscillation characteristics of gravity waves are determined and compared with the zonal oscillation of characteristics of the ionosphere.

Determining the vertical wavelength of gravity waves is very important and it is usually done using Continuous Wavelet Transform (CWT) analysis on a single temperature profile [51]. This technique is applied in this study, and it presented as

$$\text{CWT}(s, h) = \frac{1}{\sqrt{s}} \int_{-\infty}^{\infty} T_p(z) \Psi^* \left(\frac{z-h}{s} \right) dz \quad (5)$$

Ψ^* is the complex conjugate of the wavelet and it represents the scaled and translated version of the Morlet wavelet that is given by

$$\psi_o(\eta) = \pi^{-1/4} e^{i\omega_o\eta} e^{-\left(\frac{\eta^2}{2}\right)} \quad (6)$$

s and h are the scaling and translation parameters, respectively. η and ω_o are non-dimensional time and frequency, respectively. The value of ω_o is taken to be 6, in this study, as it satisfies the admissibility conditions [60]. The scaling parameter has the role of stretching or compressing the wavelets and hence it is related to the wavelength as

$$\lambda \approx \frac{4\pi s}{\omega_o + \sqrt{2 + \omega_o^2}} \quad (7)$$

Usually, the CWT is presented as a Wavelet Power Spectrum (WPS), to determine the wavelength corresponding to the dominant power of the temperature fluctuation and it is expressed as

$$\text{WPS}_{s,h} = |\text{CWT}(s, h)|^2 \quad (8)$$

The height integral of the WPS is known as the Global Wavelet Power Spectrum (GWPS), which is also a good tool to understand the dominant wavelength of the gravity wave, and it is given by

$$\text{GWPS}(s) = \int |\text{CWT}(s, h)| dh \quad (9)$$

In applying this wavelet analysis technique, the edge effect has been assessed following the technique described in [60]. Wavelet power spectrum that is contaminated by the edge effect is discarded when computing GWPS. Additionally, taking the red noise PSD as a reference, a significance test has been applied to the power spectrum of the wavelet transform. The Matlab, code available at <http://paos.colorado.edu/research/wavelets/>, accessed on 31 July 2022 (or <https://github.com/chris-torrence/wavelets>, accessed on 31 July 2022), is adopted for wavelet analysis in this study.

2.2.2. Horizontal Wavelength Estimation of Gravity Waves

Gravity waves also oscillate horizontally and, hence, their effect can be easily detected in the oscillation of the ionized atmosphere. So, it is essential to investigate and compare the characteristics of horizontal oscillation of gravity waves (from temperature profiles) and the oscillation of the ionosphere (from ion density measurements). Techniques for estimating the horizontal wavelength of a gravity wave from a pair of temperature profiles have been presented in different atmospheric dynamics studies [51,61]. Ref. [51] recommended that two temperature profiles separated by less than 300 km, obtained within less than 15 min, and the difference of their vertical wavelength of less than 6 km are useful to estimate the horizontal wavelength of a gravity wave. Two consecutive TIMED temperature profiles are provided within less than 2 min. We also have computed the separation distances between locations of two profiles that are used for horizontal wavelength estimation. About 94% of the separation distances that we found were between 200 and 300 km; the remaining fraction is for the case with a 93 km separation distance. Additionally, the maximum vertical wavelength difference among pairs of temperature profiles is about 4 km (see

Table 1) which nicely satisfies the criteria set by [51]. A pair of profiles that satisfied the above criteria is first filtered to remove the vertical wavelength above 13 km and then a pair of profiles is used, applying cross wavelet analysis, to estimate horizontal wavelengths of gravity waves. Removal of wavelengths above 13 km has been done because, in this study, gravity waves with longer vertical wavelengths are found to dissipate energy in the ionosphere-thermosphere system (above 90 km). The wavelet coherence between the two temperature perturbation profiles (T_{pa} and T_{pb}) is expressed as

$$WC_{a,b} = |WC_{a,b}| \exp(i\Phi_{a,b}) \quad (10)$$

where $\Phi_{a,b}$ is the phase difference between the two temperature profiles and it can be computed using

$$\Phi_{a,b} = \tan^{-1} \left(\frac{Im(WC_{a,b})}{Re(WC_{a,b})} \right) \quad (11)$$

where Im and Re represent imaginary and real components. The values of the phase angles within $(0, 90)$ represent the in-phase motion of the two waves while wave a leads b whereas the phase angles within $(-90, 0)$ represent in-phase motion where b leads a . The phase difference that can be obtained from Equation (11) can be related to the horizontal wave number [47,52]

$$k_H = \frac{\Phi_{a,b}}{D_{a,b}} \quad (12)$$

where $D_{a,b}$ is the distance between the location of the two profiles. Horizontal wavelength along the track of the TIMED satellite can be derived from this horizontal wave number

$$\lambda_h = \left(\frac{2\pi}{\Phi_{a,b}} \right) D_{a,b} \quad (13)$$

As can be seen from this relation, small phase shift values can result in unrealistic values of horizontal wavelength. To minimize this problem, [52] did not use phase shifts less than 30 degrees in their horizontal wavelength estimation. This angle is used as a threshold in computing the horizontal wavelength in this study too. Since either of the two profiles can be taken as a reference for phase estimation, it is expected to see mirror images when the horizontal wavelength is presented as a function of phase angles. As TIMED is orbiting with an inclination angle of 74° , the horizontal wavelength estimated using pair of profiles along the orbital plane is aligned almost meridionally. This wavelength can be mapped either along the east-west or south-north line. The east-west component can be found using the relation

$$\lambda_{zon} = \lambda_h \cos(74^\circ) \quad (14)$$

The horizontal wavelength of the oscillation of the ionospheric irregularity is estimated from the C/NOFS satellite ion density observations. Using an approach similar to that for the temperature profiles, the background ion density has been estimated by fitting a second-order polynomial to the ion density observed between 18:00 and 24:00 local time. The ion density perturbation is obtained by subtracting the background ion density from the original measurements. The ion density perturbation is analyzed using the wavelet analysis techniques described above and zonal wavelengths of the oscillation of the ion density are estimated. Finally, comparisons are made between the zonal wavelength corresponding to the dominant wavelet power of ion oscillation and the east-west component of horizontal wavelengths of gravity waves estimated for a range of phase shift angles such as from 90 to 30° (-90 to -30°) for each pair of temperature fluctuations.

3. Results

The Ion velocity meter (IVM) onboard C/NOFS has been used to measure ion density and plasma drift velocity at the equatorial ionosphere [36]. These parameters together with neutral atmospheric temperature profile observation by TIMED are used to identify the

role of gravity waves on the formation of ESF. Figures 1–3 portray in-situ ion density and vertical drift velocity (first and second rows from the top) as a function of local time (LT) at the satellite position. The last row shows trajectories of C/NOFS (dotted lines), magnetic dip equator (magenta lines), and locations where temperature profiles are obtained from TIMED (asterisks). The TIMED trajectories are obtained between 17:00 and 19:30 LT for each pass. The coordinates of temperature profiles from the TIMED satellite and the trajectory of C/NOFS indicate the availability of concurrent atmospheric temperature and ionospheric measurements. Each column represents a single orbit of C/NOFS or TIMED. In Figures 1 and 2, six orbits are presented for each whereas in Figure 3, four orbits are displayed. Figures 1 and 2 display sample results from an irregular equatorial ionosphere whereas Figure 3 shows sample results for a non-irregular and irregular equatorial ionosphere. The LT variation of the ion density and drift velocities presented in Figures 1–3 show different patterns. In Figures 1 and 2, and the third and fourth panels of Figure 3, between about 17:00 and 19:00 LT, the drift velocities are upward and increase in general with time. Slightly before 19:00 LT, the ion density started decreasing, and then after 19:00 LT continued up and down for more than two hours. The fluctuation of the ion density nicely correlates with the up and down motion of the plasma. On the other hand, in the first and second columns of Figure 3, in situ ion density decreases smoothly as time increases whereas the drift velocity points downward.

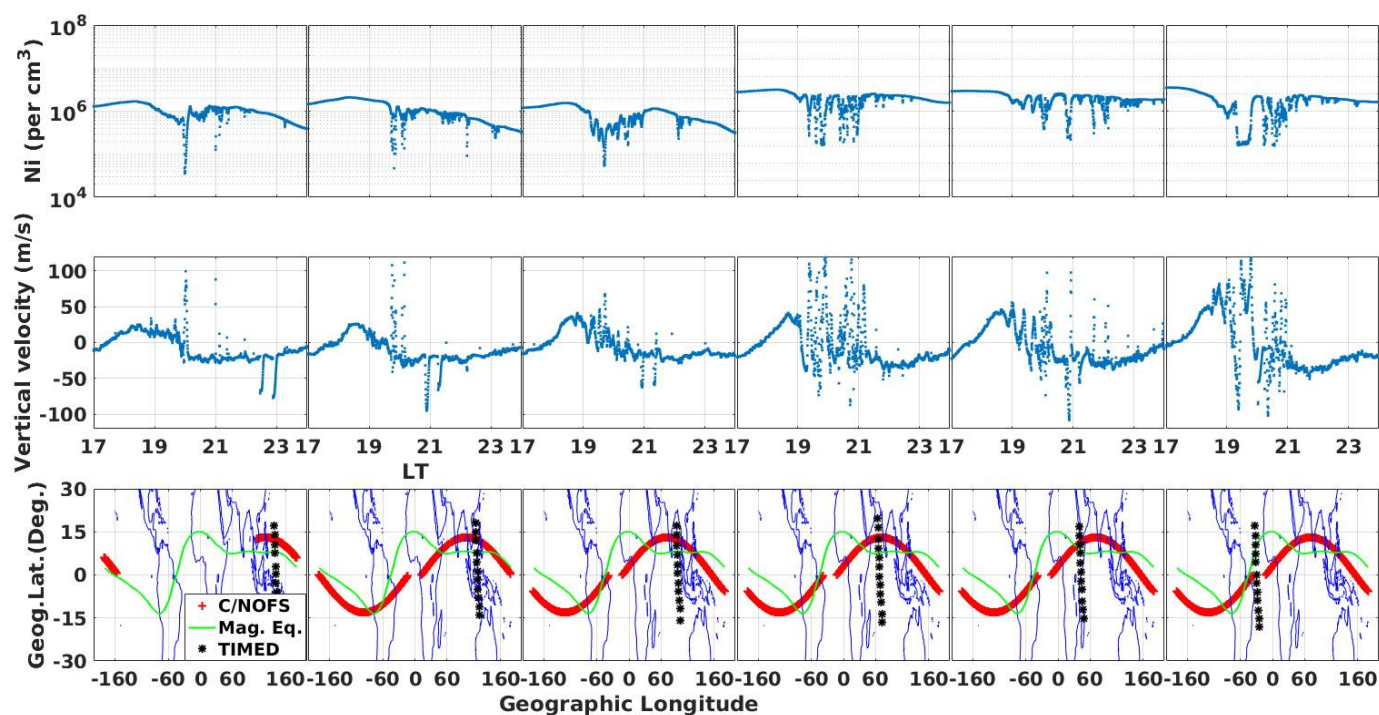


Figure 1. Irregular ion density (top row) and plasma vertical drift velocity (middle row, positive and negative values represent upward and downward, respectively) from C/NOFS and coordinates of data from C/NOFS and SABER satellites (bottom row) versus LT on 15 October 2011.

Figures 4–6 display neutral atmosphere temperature profiles obtained, in the region and time that C/NOFS provided ion density and plasma drift velocity (displayed in Figures 1–3, respectively), from TIMED and wavelet analysis results on those temperature profiles. Pair of temperature profiles shown in six (four) panels, from top to bottom, of Figures 4–6 are obtained corresponding to six (four) orbits, from left to right, of the TIMED satellite (see Figures 1–3), respectively. The normalized temperature perturbations are presented in the second column of each figure. The geographic latitude and longitude of each pair of temperature profiles corresponding to Figures 4–6 are presented in Table 1.

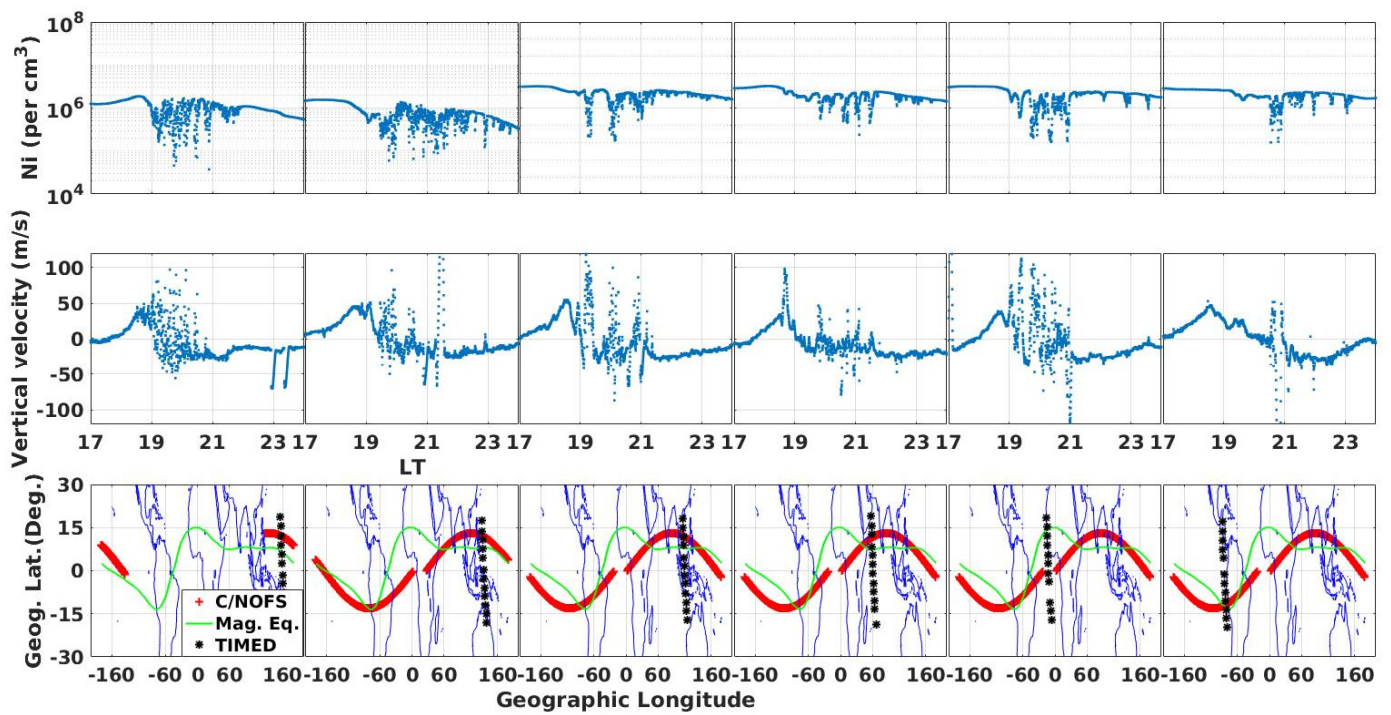


Figure 2. Irregular ion density (top row) and plasma vertical drift velocity (middle row, positive and negative values represent upward and downward, respectively) from C/NOFS and coordinates of data from C/NOFS and SABER satellites (bottom row) versus LT on 16 October 2011.

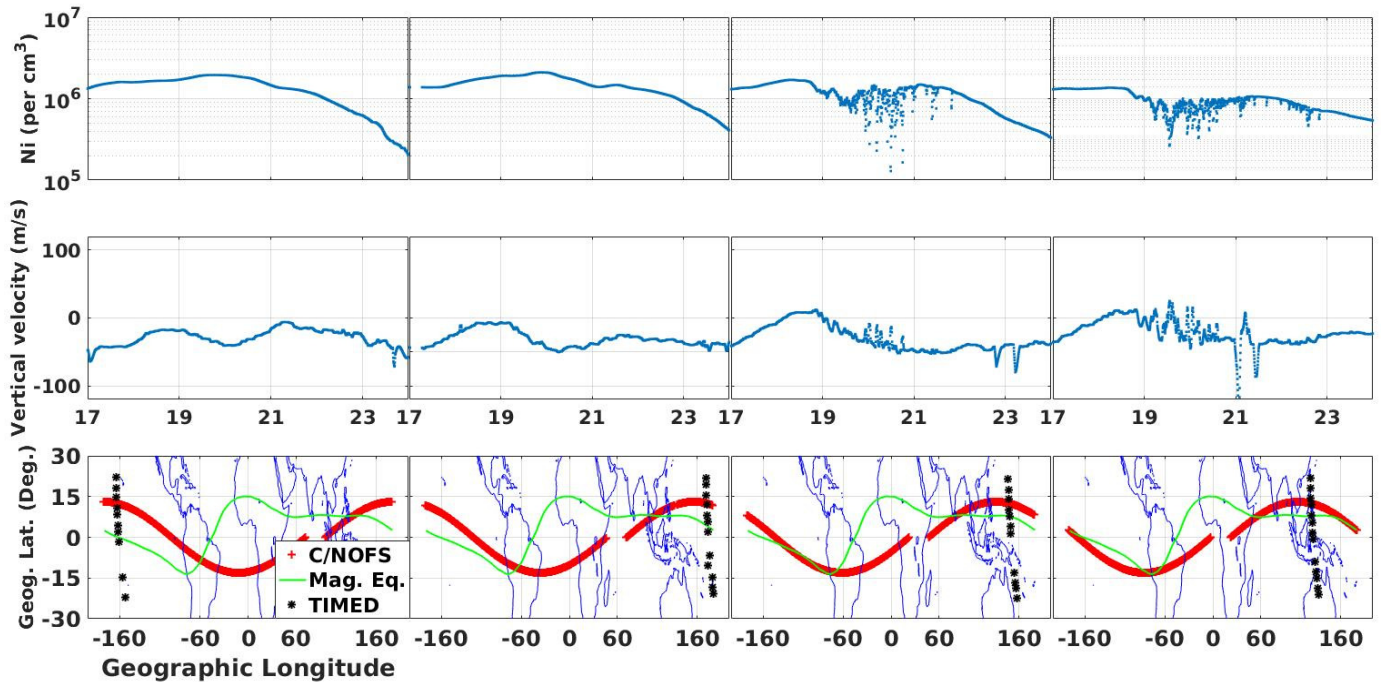


Figure 3. Ion density (top row, 1st and 2nd columns represent non-irregular ionosphere whereas 3rd and 4th columns represent irregular ionosphere) and plasma vertical drift velocity (middle row, positive and negative values represent upward and downward, respectively) from C/NOFS and coordinates of data from C/NOFS and SABER satellites (bottom row) versus LT on 14 October 2011.

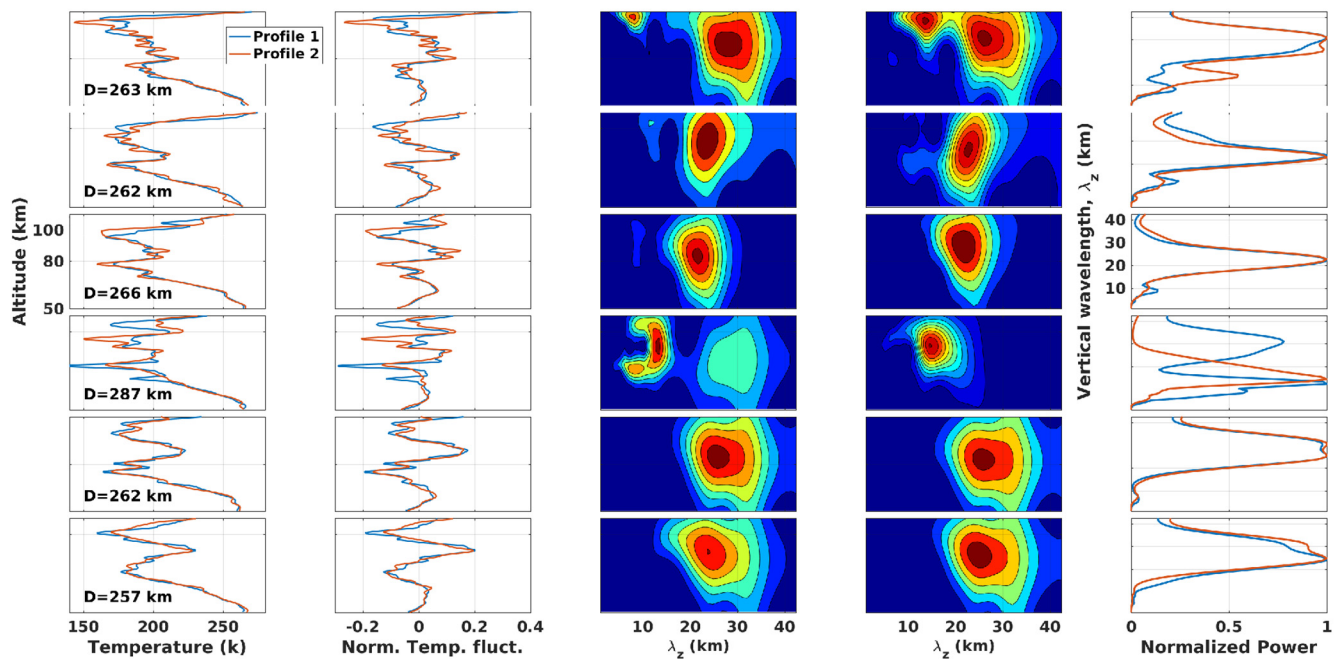


Figure 4. Temperature profiles (left panels), normalized temperature fluctuations (2nd column from the left), contour maps of WPS versus vertical wavelength and altitude for the two profiles (3rd and 4th columns from the left, deep red and blue colors represent respectively the dominant and lowest power), and normalized GWPS versus vertical wavelength (right column) corresponding to six orbits of SABER satellite on 15 October 2011.

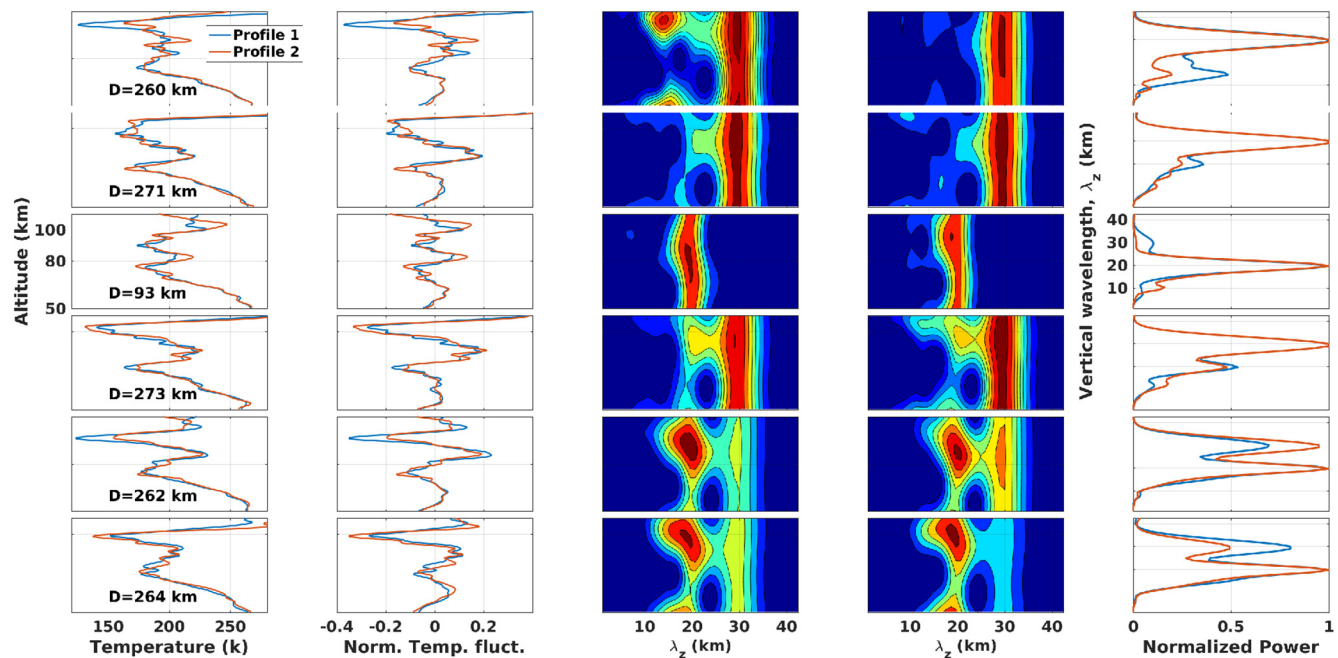


Figure 5. Temperature profiles (left panels), normalized temperature fluctuations (2nd column from the left), contour maps of WPS versus vertical wavelength and altitude for the two profiles (3rd and 4th columns from the left, deep red and blue colors represent respectively the dominant and lowest power), and normalized GWPS versus vertical wavelength (right column) corresponding to six orbits of SABER satellite on 16 October 2011.

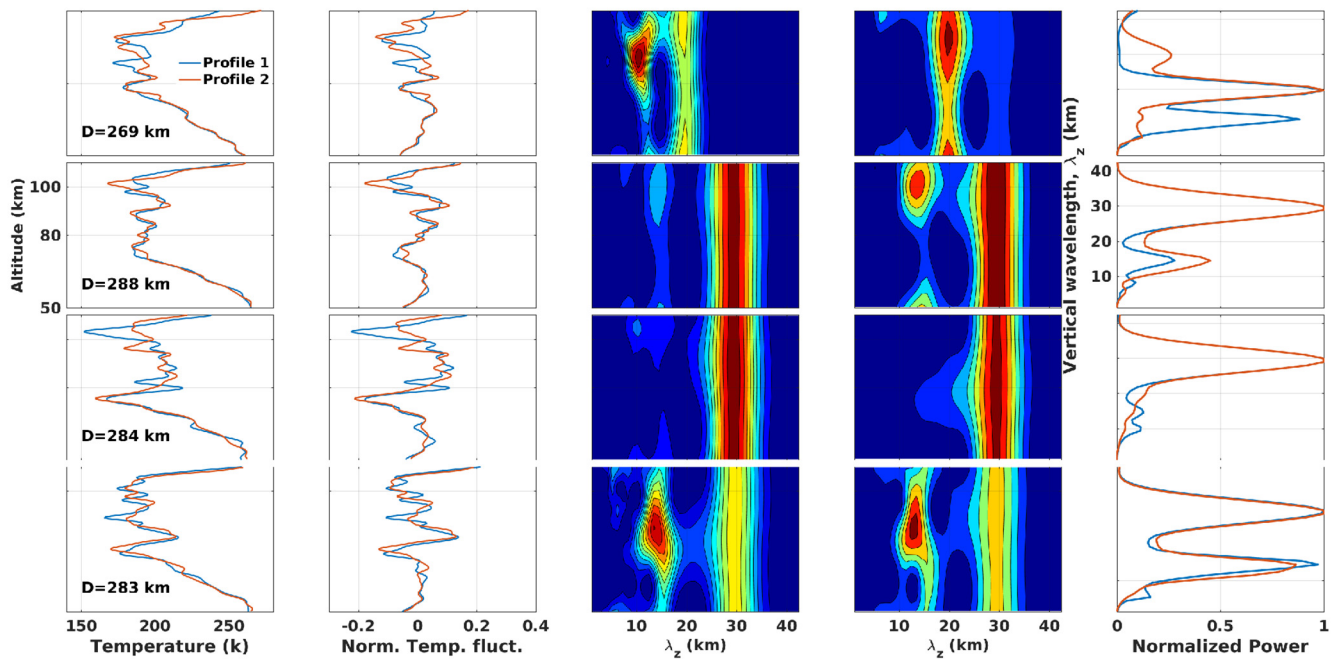


Figure 6. Temperature profiles (left panels), normalized temperature fluctuations (2nd column from the left), contour maps of WPS versus vertical wavelength and altitude for the two profiles (3rd and 4th columns from the left, deep red and blue colors represent respectively the dominant and lowest power), and normalized GWPS versus vertical wavelength (right column) corresponding to four orbits of SABER satellite on 14 October 2011.

Table 1. Geographic latitude and longitude and separation distances of pairs of temperature profiles.

TIMED Passes	Coordinates of Profile 1 (Lat. ° N, Long. ° E)	Coordinates of Profile 2 (Lat. ° N, Long. ° E)	Distance between Profiles (km)
For Figure 4			
1	(13.65, 140.30)	(11.30, 140.60)	263
2	(4.50, 117.40)	(2.20, 117.90)	262
3	(6.70, 92.40)	(4.38, 92.90)	266
4	(2.90, 68.80)	(0.40, 69.40)	287
5	(1.01, 44.70)	(−1.27, 45.28)	262
6	(−2.90, 332.20)	(−5.10, 332.90)	257
For Figure 5			
1	(8.80, 158.60)	(6.50, 159.00)	260
2	(10.70, 133.80)	(8.30, 134.20)	271
3	(1.50, 111.10)	(−0.90, 111.70)	93
4	(5.30, 61.40)	(2.90, 61.90)	273
5	(2.40, 348.60)	(0.10, 349.10)	262
6	(−4.30, 276.90)	(−6.60, 277.50)	264
For Figure 6			
1	(8.40, 196.90)	(10.80, 196.60)	269
2	(5.80, 172.90)	(8.10, 172.50)	288
3	(1.50, 149.40)	(4.00, 149.90)	284
4	(5.50, 124.10)	(8.00, 123.6)	283

The longitudes (in degree) of these temperature profiles can be categorized as 270 to 310 (America sector), 310–360 (Pacific Ocean sector), 40–60 (African sector), and 70–180 (Asian sector). These longitudes indicate the good longitudinal distribution of atmospheric temperature and ionospheric data used in this study. The distances between the pairs of temperature profiles are computed using the great circle formula and the results are presented in each panel (see the first columns of Figures 4–6 and Table 1). The distances obtained are in ranges of 257–287 km, 260–273 km, and 255–288 km for Figures 4–6, respectively, except for the third row of Figure 6 where a 93 km separation distance is obtained. These distances are less than 300 km, which [51] suggested appropriate to use temperature perturbations to infer gravity wave properties. As is seen, the amplitude of temperature perturbations grows with altitude and reaches a maximum in the altitude range of about 70 to 80 km. In general, above these heights, the amplitude of temperature fluctuation is not growing or is decaying, and this is an indication of saturation of vertically propagating gravity waves [55]. Maximum amplitude perturbation is observed at an average altitude of around 80 km. The wavelet power contour maps of every two temperature perturbations are presented separately in the third and fourth columns, from left, of Figures 4–6. The contour maps show wavelet power versus the vertical wavelength of gravity waves and altitude. The two normalized power curves in each panel are obtained from those pairs of temperature profiles presented in the second column. Dominant wavelet powers are evidently observed from both the contour maps and normalized power curves. The approximated vertical wavelengths of gravity wave corresponding to dominant wavelet powers, for Figures 4–6 are presented in Table 2.

Table 2. Vertical wavelengths of gravity waves corresponding to dominant wavelet powers shown in Figures 4–6.

TIMED Passes	Vertical Wavelength for Profile 1, λ_z (km)	Vertical Wavelength for Profile 2, λ_z (km)	Wavelength Difference (km)
For Figure 4			
1	30.99	30.99	0.00
2	23.76	22.73	1.03
3	22.73	22.73	0.00
4	12.40	14.46	2.06
5	25.83	29.96	4.13
6	24.79	24.79	0.00
For Figure 5			
1	29.96	28.93	1.03
2	28.93	28.93	0.00
3	19.63	19.63	0.00
4	28.93	28.93	0.00
5	19.63	19.63	0.00
6	19.63	19.63	0.00
For Figure 6			
1	19.63	19.63	0.00
2	28.93	28.93	0.00
3	28.93	28.93	0.00
4	29.96	28.25	1.71

The maximum difference of the vertical wavelengths among pairs of temperature perturbations is around 4 km (see Table 2). The normalized power versus vertical wavelength, for each pair of perturbations, shows a similar pattern. The vertical wavelengths, corresponding to the dominant power, range from about 12 to 31 km. In general, for each pair, the temperature perturbation profiles, and wavelet analysis results show similar variations; however, C/NOFS observations corresponding to these figures have shown significant differences. All of the panels of Figures 1–3 show strong ion density irregularity except the first and second columns in Figure 3.

Temperature perturbations shown in Figures 4–6 are direct reflections of the atmospheric gravity waves. Since the two closely found pairs of temperature profiles in each panel are similar, taking randomly one from each pair, gravity wave parameters such as potential energy and saturated power spectral density are estimated and displayed in Figures 7–9. These figures respectively are obtained from temperature perturbation profiles shown in Figures 4–6. The top panels show gravity wave potential energy versus altitude. The potential energy increases with altitude and reaches the maximum in the altitude ranges of 80 to 100 km where maximum amplitude temperature perturbations are obtained. On average above about 80 km the potential energy decreases and in some cases, it increases and decreases again above this height (i.e., up to about 110 km). The Bottom panels show the logarithm of experimental (dotted lines) and theoretical (line) saturated gravity wave PSD versus the logarithm of the vertical wave number of gravity waves. Both the vertical wave numbers and the corresponding power spectral density displayed in these figures are estimated for altitudes above 90 km. Interestingly, in Figures 7–9, experimental PSD versus wave number shows almost an identical pattern; in addition, the experimental and theoretical PSD shows excellent agreement between $10^{-3.3}$ and $10^{-2.08}$ vertical wave numbers, which respectively correspond to about 13 and 1 km vertical wavelength of gravity waves. In all of these panels, a strong deviation between theoretical and experimental PSD is observed for vertical wave numbers less than $10^{-3.3}$ (i.e., above about 13 km vertical wavelength).

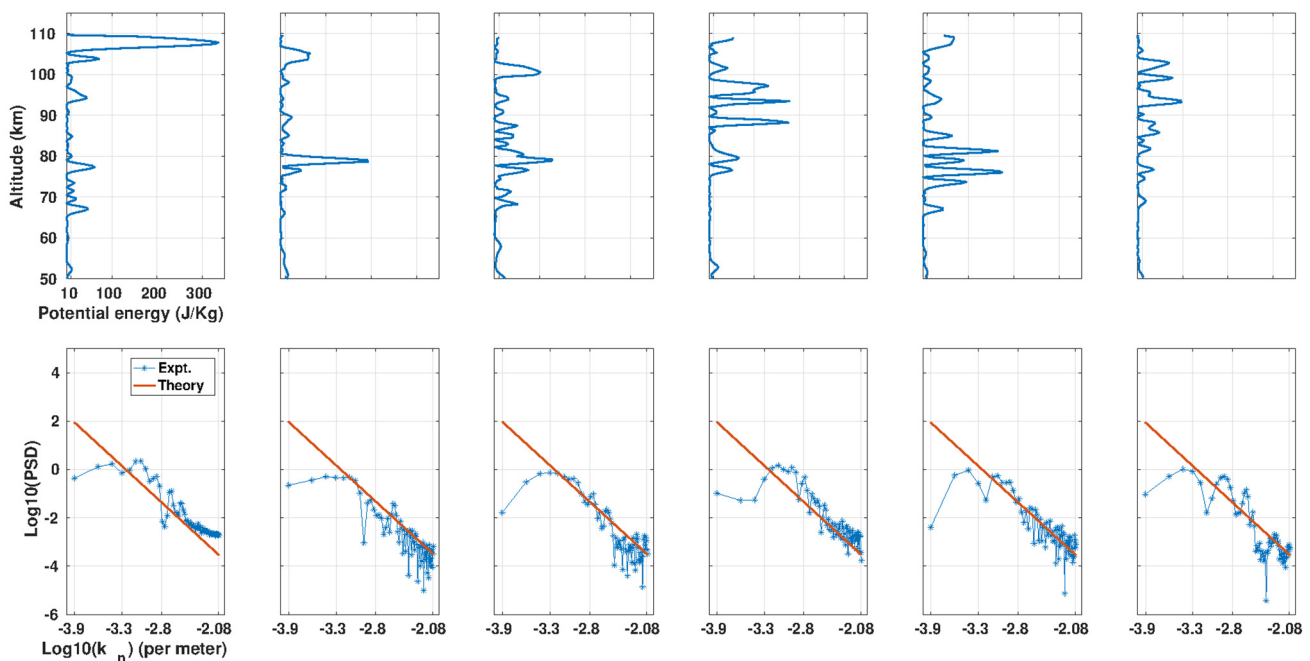


Figure 7. Potential energy of the gravity wave (top panels) versus altitude and logarithm of theoretical (red line) and experimental (lines with asterisks) power spectral density normalized temperature perturbation versus the logarithm of the vertical wave number of atmospheric gravity wave (bottom panels) on 15 October 2011.

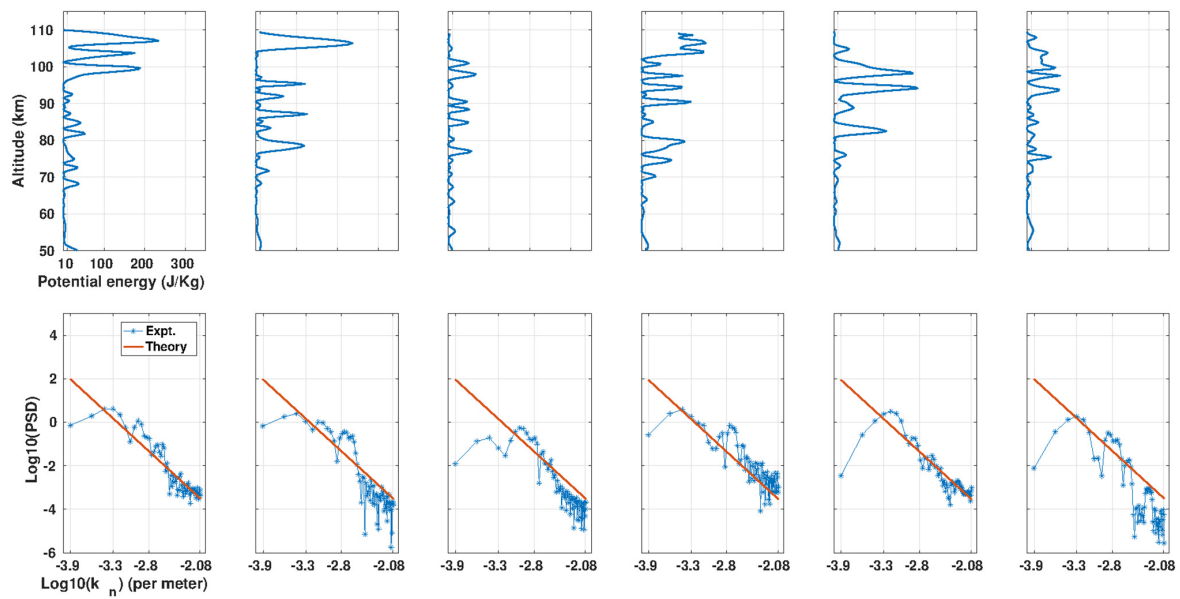


Figure 8. Potential energy of the gravity wave (**top panels**) versus altitude and logarithm of theoretical (**red line**) and experimental (**lines with asterisks**) power spectral density normalized temperature perturbation versus the logarithm of the vertical wave number of atmospheric gravity wave (**bottom panels**) on 16 October 2011.

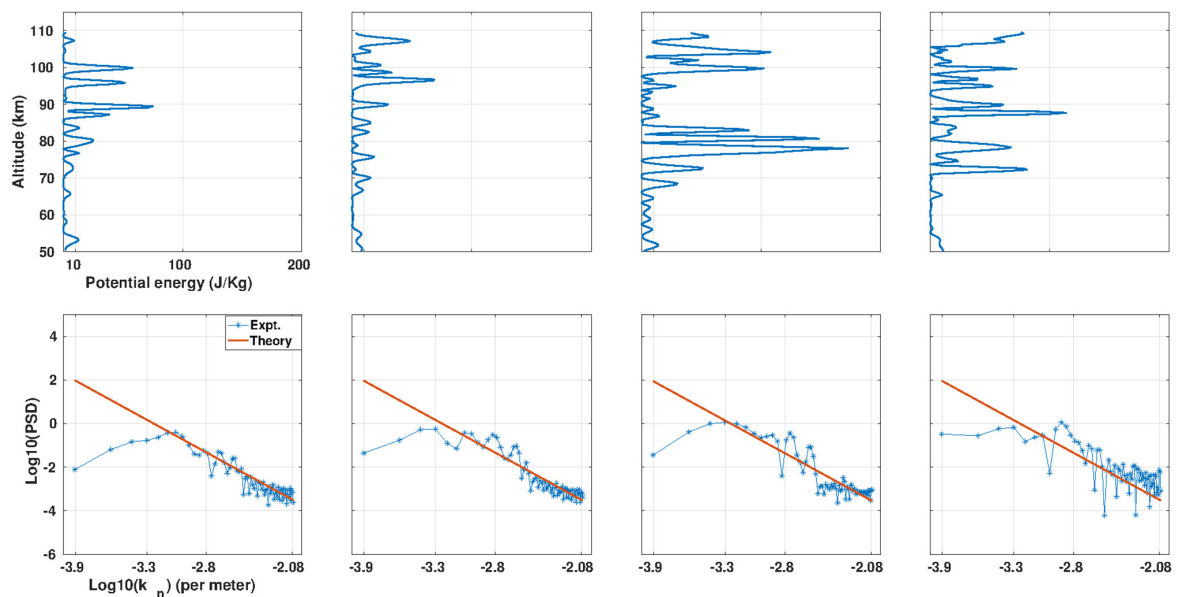


Figure 9. Potential energy of the gravity wave (**top panels**) versus altitude and logarithm of theoretical (**red line**) and experimental (**lines with asterisks**) power spectral density normalized temperature perturbation versus the logarithm of the vertical wave number of atmospheric gravity wave (**bottom panels**) on 14 October 2011.

Figures 7–9 show results corresponding to the cases presented in Figures 1–3, respectively. To complement the results presented above, 65 days of the day-to-day activity of the gravity waves are analyzed and presented in Figure 10. This figure shows all the available data in 2013 between 17:00 and 19:30 LT and -20 and 20° latitude as this study focuses on the role of gravity waves on evening time equatorial ionospheric irregularity. Within these time and latitude intervals temperature profiles are found in five months (April, June, August, October, and December 2013). In these months respectively, 15, 12, 13, 12, and

13 days of data are obtained. The day-to-day altitude variations of the potential energy show similar patterns within and across these months. As can be seen in the figure average potential energy for April, June, August, October, and December increase with altitude up to about 75, 80, 85, 80, and 80 km altitudes, respectively, and then decreases (or not growing) with increasing altitude up to about 100 km. In some cases, shortly above 100 km, it tends to increase and then immediately decreases. In general, the potential energy decreases above an average altitude of about 80 km. The logarithm of daily and mean experimental PSD of temperature fluctuations corresponding to the top panels of this figure and daily theoretical linear saturation of gravity waves PSD versus the logarithm of vertical wave number are also shown in the bottom panels of the same figure. The PSD and vertical wave numbers are also estimated corresponding to temperature fluctuations obtained above 90 km altitude. Very interestingly the experimental day-to-day values of the PSD within and among the months show similar patterns. The experimental mean PSD and the theoretical values show excellent agreement between -3.3 and -2.08 logarithm of vertical wave numbers that respectively correspond to 13 and 1 km vertical wavelength in all of the months; however, the agreement observed for June shows a slight difference compared to the other months. These plots of PSD are almost identical to the ones presented in Figures 7–9. The temperature profiles for those months are obtained from different geographic longitudes. Data for April, June, August, October, and December are obtained from longitudes ranging from 203 to 270, 10 to 49, 20 to 65, 10 to 52, and 15 to 66°, respectively. So, these longitudes can be categorized as the American sector (203–270° W) and the African sector (10–66° E). The results across these months indicate that the American and African sector gravity waves show similar activities. This is also in agreement with the ones shown in Figures 7–9.

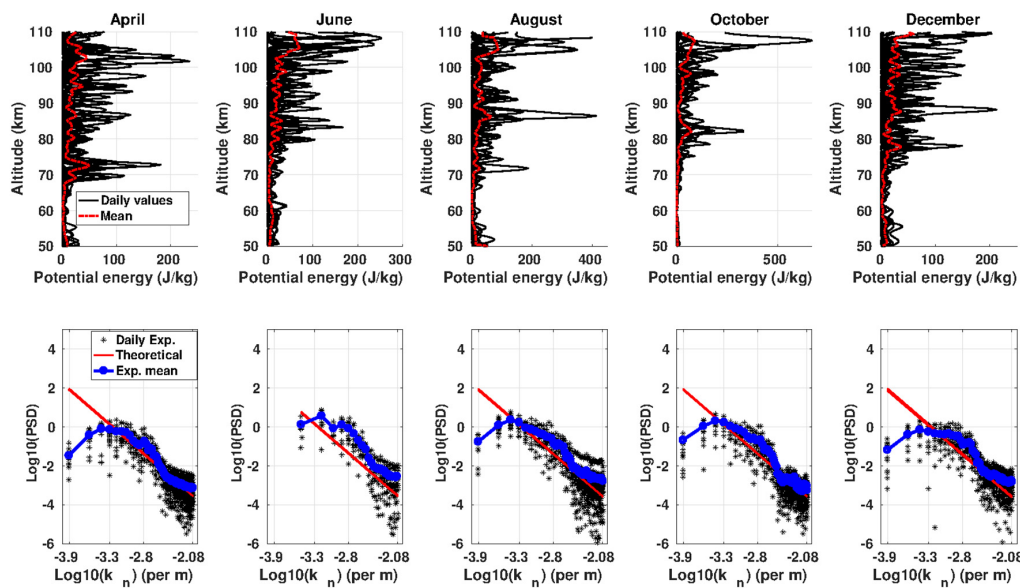


Figure 10. Gravity wave potential energy versus altitude (km) (**top panels**) and logarithm of theoretical and experimental PSD versus logarithm of vertical wave number (**bottom panels**) in the year 2013. The top panels show daily (black lines) and mean (red broken line) gravity wave potential energy versus altitude for each month.

Figures 11–13 show east-west oscillation characteristics of the ion density and atmospheric gravity waves both for the cases of irregular and non-irregular ionosphere. As clearly seen in the figure, the dominant powers that have been obtained for the cases of the irregular ionosphere are significant. Pair of tilted dotted lines (green color) overplotted on these wavelet powers indicate the cone of influence of the edges during wavelet analysis. The wavelet power within these pair of dotted lines is likely not contaminated by the edging effect. The normalized global wavelet power (shown in the third column, from the left) is obtained only by considering the wavelet power found within the cone of influ-

ence. As suggested from normalized global wavelet power plots, ion density oscillations exhibit different dominant power indicating the existence of different east-west oscillation modes of the irregularity (i.e., different horizontal wavelengths for ion density irregularity oscillations). Wavelengths corresponding to dominant power are indicated by asterisks. The fourth column, from the left, in Figures 11–13 shows the east-west component of the horizontal wavelength of atmospheric gravity waves estimated from a pair of temperature profiles versus phase shift angle. As can be seen for both the cases of irregular and non-irregular ionosphere, the east-west gravity wave wavelengths are similar; however, ion density perturbation zonal wavelengths estimated for these cases are quite different.

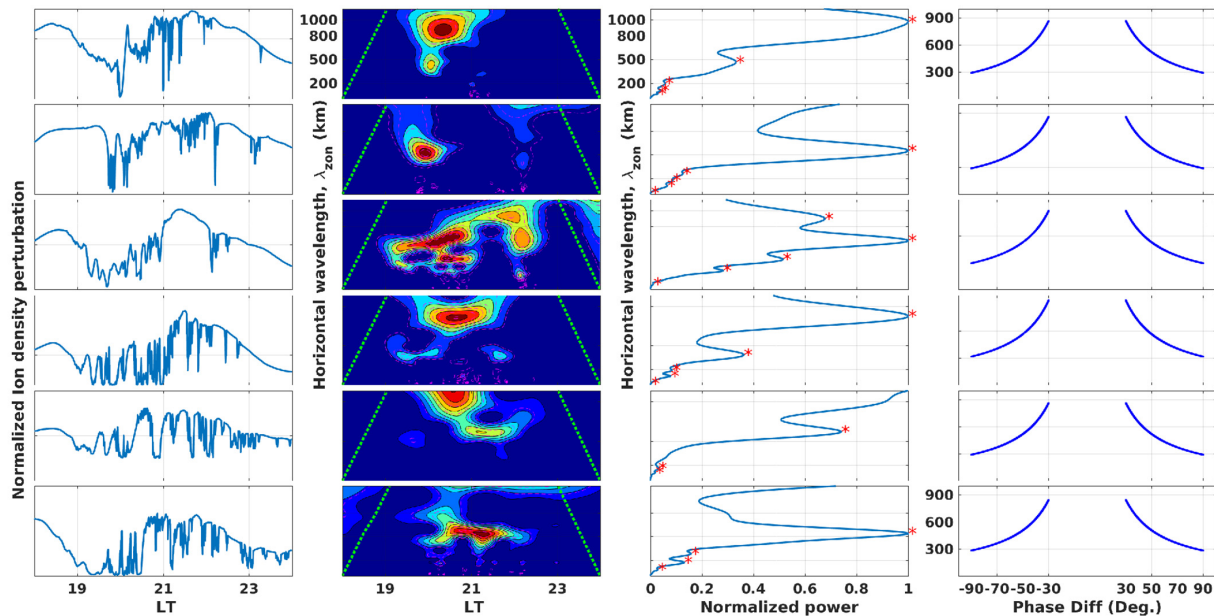


Figure 11. Normalized ion density perturbation (**left panels**) versus LT, contour map of wavelet power of normalized ion density fluctuations versus zonal wavelength and LT (**2nd column from the left**, deep red and blue colors represent dominant and weak power, 95% confidence intervals are represented by magenta color dashed line curves) and time integrated normalized wavelet power of normalized ion density fluctuations versus zonal wavelength (**3rd column from the left**), and gravity wave zonal wavelength versus phase shift (**4th column from the left**) on 15 October 2011. The asterisks in the third column represent peak value of time integrated normalized wavelet power.

Figure 14 shows the box-and-whisker (distribution) of zonal wavelengths estimated for ion density perturbations and atmospheric gravity waves. Zonal wavelengths estimated for ion density oscillation are classified into two: wavelengths below and above 143 km. The median, maximum and minimum values for the distribution of zonal wavelengths less than 143 km are 68.5 km, 113 km, and about 16 km, respectively (see top left panel). For the distribution of zonal wavelengths above 143 km, the median, maximum, and minimum values are 491 km, 1520 km, and 146 km, respectively (see top right panel). The bottom left and right panels also show the zonal wavelength of atmospheric gravity waves for the cases of irregular and non-irregular ionosphere, respectively. As can be seen during the irregular condition, the median, maximum, and minimum east-west atmospheric gravity wavelengths are 518 km, 944 km, and 282 km, respectively. During the non-irregular situation, the median, maximum, and minimum zonal atmospheric gravity wave wavelengths are 495 km, 947 km, and 296 km, respectively. These results show that the median values of the zonal wavelength of gravity waves corresponding to irregular and non-irregular conditions of the ionosphere are similar. These median values are also in better agreement with the median value of the zonal wavelengths (for the cases above 143 km) estimated for the irregular conditions of the ionosphere than for non-irregular conditions of the ionosphere.

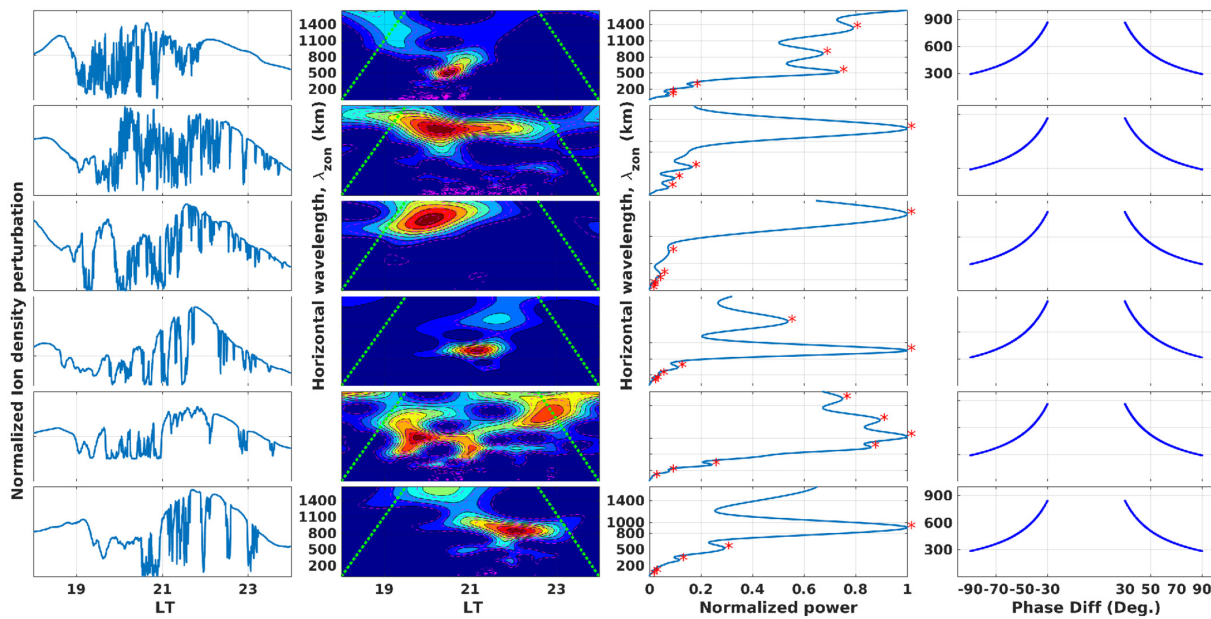


Figure 12. Normalized ion density perturbation (**left panels**) versus LT, contour map of wavelet power of normalized ion density fluctuations versus zonal wavelength and LT (**2nd column from the left**, deep red and blue colors represent dominant and weak power, 95% confidence intervals are represented by magenta color dashed line curves) and time integrated normalized wavelet power of normalized ion density fluctuations versus zonal wavelength (**3rd column from the left**), and gravity wave zonal wavelength versus phase shift (**4th column from the left**) on 16 October 2011. The asterisks in the third column represent peak value of time integrated normalized wavelet power.

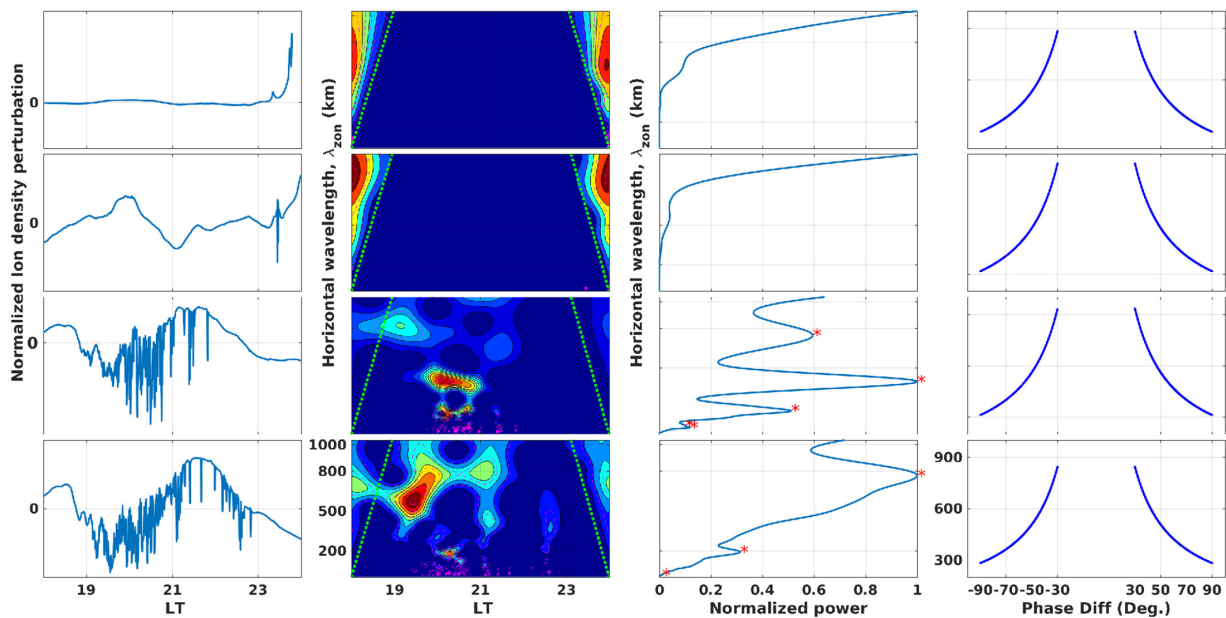


Figure 13. Normalized ion density perturbation (**left panels**) for non-irregular (**1st and 2nd rows**) and irregular (**3rd and 4th rows**) versus LT, contour map of wavelet power of normalized ion density fluctuations shown in the 1st column versus zonal wavelength and LT (**2nd column from the left**, deep red and blue colors represent dominant and weak power, 95% confidence intervals are represented by magenta color dashed line curves) and time integrated normalized wavelet power of normalized ion density fluctuations versus zonal wavelength (**3rd column from the left**), and gravity wave zonal wavelength versus phase shift (**4th column from the left**) on 14 October 2011. The asterisks in the third column represent peak value of time integrated normalized wavelet power.

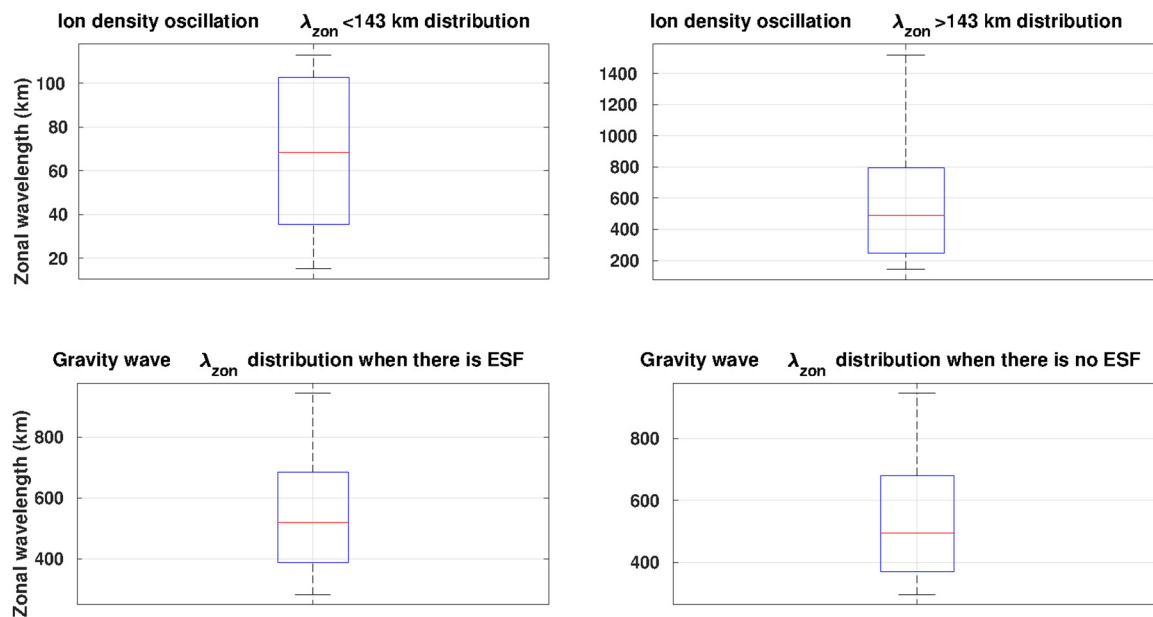


Figure 14. Box-and-whisker of zonal wavelengths of ion density perturbation for the cases less than (**top left**) and greater than (**top right**) 143 km wavelengths and atmospheric gravity waves for the cases of irregular (**bottom left**) and non-irregular (**bottom right**) ionosphere.

4. Discussion

Gravity wave seeded Rayleigh-Taylor Instability is considered a cause of the day-to-day variation in the occurrence of equatorial ionospheric irregularity [7,18,24,33–35]. Gravity wave characteristics are usually estimated from ionospheric irregularity observations [10,62,63]. However, many things remain unclear in understanding the role of gravity waves in ionospheric irregularity. For example, as gravity waves have a broad spectrum, the specific gravity waves that cause ionospheric irregularity are not clearly known using both gravity waves and ionospheric measurements. In addition, the relationship between the characteristics of zonal oscillation of gravity waves and zonal wavelength of ionospheric irregularities has not yet been investigated using both atmospheric and ionospheric observations. In lower and middle atmospheric dynamics studies, variations of temperature, neutral density, and wind speed are used to characterize gravity waves that propagate in the ionosphere-thermosphere system and in the Earth's lower atmosphere [27,54]. For this study, the MLT (Mesosphere Lower Thermosphere) temperature perturbation profiles obtained from the TIMED satellite are taken as gravity wave indicators while ionospheric ion density and vertical drift velocity observations from the C/NOFS satellite are used to characterize equatorial ionospheric irregularity. Spectral and wavelet analysis techniques mainly are used to address the objectives set for this study.

Different studies have applied wavelet analysis to investigate basic parameters of gravity waves on single and pairs of temperature profiles [51]. Applying similar techniques on single temperature profile gravity wave characteristics are presented in Figures 4–6. For the cases of irregular and non-irregular ionosphere (Figures 1–3), the vertical wavelength of gravity waves, associated with the dominant power, varies from about 12 to 31 km. The vertical wavelengths estimated for both cases are very similar to the previous studies carried out to understand the effect of gravity waves on the dynamics and structure of the middle atmosphere [46,48,49,64]. Furthermore, as can be seen in Table 2, the dominant vertical wavelengths estimated corresponding to the cases of irregular and non-irregular ionosphere are very similar. Potential energies of gravity waves estimated from each temperature profile have shown similar characteristics (see top panels of Figures 7–10). The potential energy of gravity waves increases with height, for both irregular and non-irregular ion density, and reaches a maximum within altitude ranges from 80 to 100 km, in

general. Similarly, within these altitude ranges amplitude of perturbation of temperature profiles increases with a height that may be due to the conservation of energy as the neutral density of the atmosphere decreases with altitude [53,54] and reaches a maximum within those height ranges. It is evident also that both the amplitude of temperature perturbation and potential energy decrease, in general, with increasing altitude above the maximum amplitude fluctuation heights (i.e., on average above about 80 km), and this result is similar to the previous findings [65]. The decay (or cessation) of the potential energies of gravity waves on average above 80 km may be due to the transfer of gravity wave energy to the ionosphere-thermosphere system [27,56]. This is because as the amplitude of gravity waves reaches the maximum, it provides irreversible energy transfer to the ionosphere-thermosphere system [55] that can provide body force to the neighboring ionosphere-thermosphere system [66]. As a result, above the height of maximum oscillation, its energy or amplitude tends to decrease as altitude increases. Gravity wave energy dissipation through convective or dynamical instability in the ionosphere-thermosphere system is usually described by the linear saturation theory [54–56].

Spectral analysis results presented in the bottom panels of Figures 7–10 show very interesting results. This spectral analysis has been done considering temperature perturbations above 90 km (as the ionosphere-thermosphere system that we have temperature observation of is the main interest). The theoretical and experimental PSD show very nice agreement within $10^{-2.08}$ and $10^{-3.3}$ vertical wave numbers that correspond to vertical wavelengths ranging from about 1 and 13 km, respectively. This indicates that gravity waves with vertical wavelengths between about 1 and 13 km are the ones that dissipate energy at heights above about 90 km in the ionosphere-atmosphere system [67]. The agreement between experimental and theoretical PSD holds true for day-to-day activity within each month and across those months (Figure 10); indicating that in the American (203 to 260° W, April month) and African (other months) longitudinal sectors similar ranges of gravity waves dissipate energy. The similar results obtained for these longitudes may be a consequence of similar processes triggering gravity waves in both sectors, for example, the passage of the solar terminator that usually happens around 18:00 LT [68]. The transfer of gravity wave energy into the ionosphere-thermosphere system on all of those days (68 days) is in agreement with the daily existence of gravity waves suggested by [62,63,69]. The similarity of gravity waves that dissipate energy in these two longitudinal sectors raises questions about the cause of the longitudinal variability of the equatorial ionospheric irregularity [21,31]. It is well documented that the African ionosphere shows a more frequent occurrence of irregularities than other longitudinal sectors in almost all seasons [31]; on the other hand, the magnitude of the vertical drift velocity, which is assumed to be the main driver of irregularities [33], for the American sector is larger than the vertical drift over Africa [21]. Perhaps the body forces of gravity waves differ in these longitudinal sectors and are the cause of the longitudinal variability of the ionospheric irregularity in these sectors, but it requires further investigation. The ionosphere-thermosphere system with altitudes less than about 300 km is identified as a location where gravity waves dissipate energy [70–73]. For example, [73] applied numerical simulations to identify the ionosphere-thermosphere system between the altitudes 120 and 230 km as the regions where vertically propagating gravity waves dissipate energy and momentum. This means our results are consistent with these previous theoretical findings.

Taking concurrent neutral temperature profiles from TIMED and ion density from C/NOFS measurements, for the first time from these two data sources, zonal wavelengths of gravity waves and ion density oscillations are estimated. For the case of the irregular ionosphere, more than two dominant zonal wavelengths of ion density perturbation are identified corresponding to each pass of the C/NOFS satellite. It is not surprising that there are no significant and edging effect-free dominant zonal wavelengths observed for the case of the non-irregular ionosphere. Similarly, by removing the components above 13 km vertical wavelength from each perturbation of temperature profile, as gravity waves with 13 km and below are obtained to dissipate energy in the ionosphere-thermosphere system

above 90 km, the zonal wavelengths along the TIMED satellite track have been obtained using Equation (14). The horizontal wavelength along the TIMED satellite track is projected along the east-west direction using its orbital inclination angle as a mapping function as given in Equation (14). The gravity waves' horizontal wavelength along the east-west, obtained for the case of irregular and non-irregular ion density, are displayed in the fourth column, from left in Figures 11–13. The average horizontal distance between temperature profiles considered in this study is $D_{a,b} \approx 260$ km. This means that the correct horizontal wavelengths of the gravity waves are the ones longer than the Nyquist wavelength which is $\lambda_{nq} = 2 D_{a,b}$ (≈ 520 km) along the TIMED track [48]. Therefore, the minimum east-west wavelength of gravity waves from the temperature samples taken in this study is expected to be about 143 km (≈ 520 km $\times \cos(74^\circ)$). Interestingly the minimum horizontal wavelength that has been estimated using the wavelet coherency technique and Equations (13) and (14) is about twice the Nyquist wavelength (see the minimum values of horizontal wavelengths shown in the fourth columns of Figures 11–13).

The distribution (box-and-whisker) of zonal wavelengths estimated corresponding to dominate wavelet power of ion density irregularities (the one shown by asterisks in the third columns of Figures 11–13) and pairs of temperature perturbations are presented in Figure 14. These results are in agreement with the findings obtained by different studies. For example, [74], analyzing the Atmosphere Explorer E data, found mostly 150–800 km east-west wavelengths. Similarly, from equatorial Atmosphere radar data in the Indonesian sector, the distances between adjacent plasma bubbles are found to be within 370 to 1000 km [30]. Additionally, [29], analyzing ROCSAT-1 and IMAGE satellites data, found 300–1000 km average distances within the plasma bubbles. Relatively short zonal wavelengths (i.e., less than 113 km) estimated to correspond to the dominant wavelet power of ion density perturbations are also in agreement with the results shown by [10,31] and the references therein. These indicate that the wavelengths of the ion density perturbations that have been estimated in the current study nicely correlate with previous findings. The left and right bottom panels of Figure 14 are also depicting the box plot of zonal horizontal wavelengths of gravity waves estimated for the cases of irregular and non-irregular ionosphere, respectively. Interestingly the minimum, maximum, and median values of the zonal wavelength of gravity waves for irregular and non-irregular cases are very similar. Furthermore, the median values of wavelengths above 143 km for irregular ion density, for gravity waves during irregular ionosphere, and for gravity waves during non-irregular ionosphere are about 491 km, 518 km, and 495 km, respectively. This interesting agreement is found, for the first time, between the zonal characteristics of the atmospheric gravity waves and ion density irregularities.

The cause-and-effect relations between gravity waves and irregularity of the ions can be explained as follows. The spectral analysis results shown above indicate that gravity waves with vertical wavelengths less than or equal to 13 km dissipate energy above 90 km in the ionosphere-thermosphere system. When these waves dissipate energy there will be body force on the ionosphere-thermosphere system [70,72]. It is known that dissipated energy can modulate (or accelerate) the neutral winds in the ionosphere-thermosphere system below 300 km [66]. As neutral winds are forced to move in the Earth's magnetic field, there will be polarized electric fields [75,76] that can be mapped to higher altitudes (bottom of F-layer) over the magnetic equator and induce oscillation of ions with a similar zonal wavelength of the atmospheric gravity waves as is found in this study. Or, while the gravity waves with vertical wavelengths of less than or equal to 13 km dissipate energy at around 100 km, secondary waves with a similar range of vertical wavelengths can propagate to higher altitudes (around 250 km) and dissipate energy that could generate body force there and create the oscillations of ion density either due to induced polarized electric field or by direct disturbance of the ionization itself [73,76]. The east-west horizontal wavelengths that are obtained for both ion density irregularities and atmospheric gravity waves, in the current study, are within the horizontal wavelengths estimated theoretically from the secondary waves; may be the upward or downward propagating gravity waves induce

horizontally propagating irregularities in the ionosphere electron density with horizontal wavelengths of 100–4000 km. Ref. [73] p. 2599 describe “horizontal and vertical velocities induced by the primary GWs”. As is shown in spectral analysis results, the ionosphere-thermosphere system is impacted every day by atmospheric gravity waves; indicating that seeding of gravity waves exists every day; however, irregularities were not observed every evening in all equatorial longitudes. The disappearance of ionospheric irregularities as shown in the first and second columns of Figure 3 might be due to the stabilization of gravity wave seed perturbation by the downward motion of the plasma. In the remaining cases when there were irregularities, the gravity wave seed perturbation is amplified and raised to higher altitudes by upward vertical drift velocity of plasma. However, the range of gravity waves that can be the cause for the formation of ionospheric irregularity in this study is different from the one suggested by [77] carrying out numerical simulations and this difference requires further investigation.

5. Conclusions

In this study, the MLT temperature profiles from the TIMED satellite and ion and drift velocities with and without irregularities from C/NOFS satellites have been examined to identify the range of internal gravity waves responsible for seeding the ESF where those gravity waves dissipate energy. In addition to identifying the day-to-day and longitudinal variability of gravity waves from 65 days of temperature profiles in the year 2013 within 17:00 and 19:30 LT and -20 and 20° of latitude have been analyzed. Using these atmospheric and ionospheric data, the oscillation characteristics of gravity waves and ion density irregularities are estimated and compared by applying wavelet analysis techniques. Based on the analysis results the following conclusions are drawn. Gravity waves with vertical wavelengths from 1 to 13 km dissipate energy in the altitude ranges of 90 to 110 km. Additionally, these gravity waves show similar spectral characteristics for the American and African longitudinal sectors. It seems likely that vertically propagating gravity waves sweep the lower thermosphere daily with similar characteristics. The zonal wavelength of atmospheric gravity waves estimated from pairs of temperature profiles separated by 200 to 300 km for phase shift angles from 30 to 90 degrees is found to be between about 290 and 950 km regardless of the condition of the ionosphere. The median zonal wavelength of gravity waves for the cases of irregular and non-irregular ionosphere respectively are found to be 518 and 495 km. Similarly, zonal wavelengths of ion density perturbations correspond to below and above Nyquist zonal wavelength of gravity waves from about 16 to 113 km and from 146 to 1520 km, and the median values are 69 and 491 km, respectively. The median values of zonal wavelengths of gravity waves (corresponding to both irregular and non-irregular ionosphere) and ion density perturbation for the case above Nyquist wavelength have shown excellent agreement. These results indicate that vertically propagating gravity waves with vertical wavelengths from about 1 to 13 km are the ones that trigger the initial perturbation of ion density that is used as a seed for ESF development. Therefore, the integration of energy dissipation and momentum flux of those ranges of gravity waves in numerical, empirical, and physical modeling of ESF is recommended.

Author Contributions: Conceptualization, investigation, writing—draft preparation of manuscript, M.N., supervision, writing—review and editing, M.M. and E.Y. All authors have read and agreed to the published version of the manuscript.

Funding: This research was funded by Air Force Office of Scientific Research and Air Force Material Command USAF under Award No. FA8655-22-1-0001.

Institutional Review Board Statement: Not applicable.

Informed Consent Statement: Not applicable.

Data Availability Statement: All the data used are online available for public use. C/NOFS data can be accessed from <https://cdaweb.gsfc.nasa.gov/pub/data/cnofs/> (accessed on 31 July 2022) whereas data from TIMED/SABER can be accessed from <https://cdaweb.gsfc.nasa.gov/pub/data/timed/saber/> (accessed on 31 July 2022).

Acknowledgments: Melessew Nigussie's work is partially supported by the Air Force Office of Scientific Research and Air Force Material Command USAF under Award No. FA8655-22-1-0001. Moreover, Melessew Nigussie is grateful to the University of Michigan African Presidential Scholarship (UMAPS) Program and the University of Michigan for their support and hospitality in doing part of this work. CINDI data are provided through the auspices of the CINDI team at the University of Texas at Dallas supported by NASA grant NAS5-01068, the authors thank the CINDI investigator team. Additionally, the authors thank the TIMED/SABER satellite team for providing temperature profile data. Endawoke Yizengaw's work has been partially supported by AFOSR (FA9550-20-1-0119) and NSF (AGS-1848730) grants. Mark Moldwin's work is partially supported by AGS-1848724. We would like to thank Jaya Prakash Raju who indicated to us where to get temperature profile data.

Conflicts of Interest: The authors confirm there is no conflict of interest.

References

- Booker, H.G.; Wells, H.W. Scattering of radio waves by the F-region of the ionosphere. *Terr. Magn. Atmos. Electr.* **1938**, *43*, 3. [[CrossRef](#)]
- Fejer, B.G.; de Paula, E.R.; González, S.A.; Woodman, R.F. Average vertical and zonal F region plasma drifts over Jicamarca. *J. Geophys. Res.* **1991**, *96*, 13901–13906. [[CrossRef](#)]
- Zalesak, S.T.; Ossakow, S.L.; Chaturvedi, P.K. Nonlinear Equatorial Spread F: The Effect of Neutral Winds and Background Pedersen Conductivity. *J. Geophys. Res.* **1982**, *87*, 151–166. [[CrossRef](#)]
- Dungey, J.W. Convective diffusion in the equatorial F-region. *J. Atmos. Sol. Terr. Phys.* **1956**, *9*, 304–310. [[CrossRef](#)]
- Kelley, M.C.; Haerendel, G.; Kappler, H.; Valenzuela, A.; Balsley, B.B.; Carter, D.A.; Ecklund, W.L.; Carlson, C.W.; Hausler, B.; Torbert, R. Evidence for a Rayleigh-Taylor type instability and upwelling of depleted density regions during equatorial spread F. *Geophys. Res. Lett.* **1976**, *3*, 8. [[CrossRef](#)]
- Woodman, R.F.; la Hoz, C. Radar Observations of F region Equatorial Irregularities. *J. Geophys. Res.* **1976**, *81*, 31.
- Sultan, P.J. Linear theory and modeling of the Rayleigh-Taylor instability leading to the occurrence of equatorial spread F. *J. Geophys. Res.* **1996**, *101*, 875–891.
- Abdu, M.A.; de Medeiros, R.T.; Bitterncourt, J.A.; Batista, I.S. Vertical ionization drift velocities and range type spread F in the evening equatorial ionosphere. *J. Geophys. Res.* **1983**, *88*, 399–402. [[CrossRef](#)]
- Farley, D.T.; Alsley, B.B.; Woodman, R.F.; Lure, J.P.M. Equatorial Spread F' Implications of VHF Radar Observations. *J. Geophys. Res.* **1970**, *75*, 34.
- Kelley, M.C. Equatorial spread F: Recent results and outstanding problems. *J. Atmos. Terr. Phys.* **1985**, *47*, 745–752. [[CrossRef](#)]
- Zalesak, S.T.; Ossakow, S.L. Nonlinear Equatorial Spread F: Spatially Large Bubbles Resulting from Large Horizontal Scale Initial Perturbations. *J. Geophys. Res.* **1980**, *85*, 2131–2142. [[CrossRef](#)]
- Fejer, B.G.; Scherliess, L.; de Paula, E.R. Effects of the vertical plasma drift velocity on the generation and evolution of equatorial spread F. *J. Geophys. Res.* **1999**, *104*, 859–869.
- Jayachandran, B.; Balan, N.; Rao, P.B.; Sastri, J.H.; Bailey, G.J. HF Doppler and Ionosonde Observations on the Onset Conditions of Equatorial Spread F. *J. Geophys. Res.* **1993**, *98*, 741–750.
- Smith, J.M.; Rodrigues, F.S.; de Paula, E.R. Radar and satellite investigations of equatorial evening vertical drifts and spread F. *Ann. Geophys.* **2015**, *33*, 1403–1412. [[CrossRef](#)]
- Stolle, C.; Lühr, H.; Fejer, B.G. Relation between the occurrence rate of ESF and the equatorial vertical plasma drift velocity at sunset derived from global observations. *Ann. Geophysicae.* **2008**, *26*, 3979–3988. [[CrossRef](#)]
- Scannapieco, A.J.; Ossakow, S.L. Nonlinear equatorial spread F. *Geophys. Res. Lett.* **1976**, *3*, 8. [[CrossRef](#)]
- Maruyama, T.; Saito, S.; Kawamura, M.; Nozaki, K.; Krall, J.; Huba, J.D. Equinoctial asymmetry of a low-latitude ionosphere-thermosphere system and equatorial irregularities: Evidence for meridional wind control. *Ann. Geophys.* **2009**, *27*, 2027–2034. [[CrossRef](#)]
- Mendillo, M.; Baumgardner, J.; Pi, X.; Sultan, P.J.; Tsunoda, R. Onset Conditions for Equatorial Spread F. *J. Geophys. Res.* **1992**, *97*, 865–876.
- Susumu, S.; Takashi, M. Effects of Trans-equatorial Thermospheric Wind on Plasma Bubble Occurrences. *J. Natl. Inst. Inf. Commun. Technol.* **2009**, *56*, 1–4.
- Huba, J.D.; Krall, J. Impact of meridional winds on equatorial spread F: Revisited. *Geophys. Res. Lett.* **2013**, *40*, 1268–1272. [[CrossRef](#)]
- Yizengaw, E.; Moldwin, M.B.; Zesta, E.; Biouele, C.M.; Damtie, B.; Mebrahtu, A.; Rabi, B.; Stoneback, C.F.V.R. The longitudinal variability of equatorial electrojet and vertical drift velocity in the African and American sectors. *Ann. Geophys.* **2014**, *32*, 231–238. [[CrossRef](#)]

22. Tsunoda, R.T. Control of the Seasonal and Longitudinal occurrence of Equatorial Scintillation by the longitudinal gradient Integrated E Region Pedersen Conductivity. *J. Geophys. Res.* **1985**, *90*, 447–456. [[CrossRef](#)]
23. Tsunoda, R.T. Day-to-day variability in equatorial spread F: Is there some physics missing? *Geophys. Res. Lett.* **2006**, *33*, L16106. [[CrossRef](#)]
24. Kelley, M.C.; Larsen, M.F.; LaHoz, C.; McClure, J.P. Gravity wave initiation of equatorialspread F: A case study. *J. Geophys. Res.* **1981**, *86*, 9087–9100. [[CrossRef](#)]
25. Tsunoda, R.T. on equatorial spread F: Establishing a seeding hypothesis. *J. Geophys. Res.* **2010**, *115*, A12303. [[CrossRef](#)]
26. Hocke, K.; Schlegel, K. A review of atmospheric gravity waves and travelling ionospheric disturbances: 1982–1995. *Ann. Geophysicae.* **1996**, *14*, 917–940.
27. Hines, C.O. Internal atmospheric gravity waves at ionospheric heights. *Can. J. Phys.* **1960**, *38*, 1441–1481. [[CrossRef](#)]
28. Röttger, J. Wavelike structure of large-scale equatorial spread F irregularities. *J. Atmos. Sol-Terr. Phys.* **1973**, *35*, 1195–1206. [[CrossRef](#)]
29. Lin, S.C.; Immel, T.J.; Yeh, H.C.; Mende, S.B.; Burch, J.L. Simultaneous observations of equatorial plasma depletion by IMAGE and ROCSAT-1 satellites. *J. Geophys. Res.* **2005**, *110*, A06304. [[CrossRef](#)]
30. Fukao, S.; Yokoyama, T.; Tayama, T.; Yamamoto, M.; Maruyama, T.; Saito, S. Eastward traverse of equatorial plasma plumes observed with the Equatorial Atmosphere Radar in Indonesian sector. *Ann. Geophys.* **2006**, *24*, 1411–1418. [[CrossRef](#)]
31. Hei, M.A.; Heelis, R.A.; McClure, J.P. Seasonal and longitudinal variation of large-scale topside equatorial plasma depletions. *J. Geophys. Res.* **2005**, *110*, A12315. [[CrossRef](#)]
32. Tsunoda, R.T. On the enigma of day-to-day variability in equatorial spread F. *Geophys. Res. Lett.* **2005**, *32*, L08103. [[CrossRef](#)]
33. Abdu, M.A.; Kherani, E.A.; Batista, I.S.; de Paula, E.R.; Fritts, D.C.; Sobral, J.H.A. Gravity wave initiation of equatorial spread F/plasma bubble irregularities based on observational data from the SpreadFEx campaign. *Ann. Geophys.* **2009**, *27*, 2607–2622. [[CrossRef](#)]
34. Huang, C.S.; Kelley, M.C. Nonlinear evolution of equatorial spread F1. On the role of plasma instabilities and spatial resonance associated with gravity wave seeding. *J. Geophys. Res.* **1996**, *101*, 283–292. [[CrossRef](#)]
35. Huang, C.S.; Kelley, M.C. Nonlinear evolution of equatorial spread F2. Grvity wave seeding of Rayleigh-Taylor instability. *J. Geophys. Res.* **1996**, *101*, 293–302. [[CrossRef](#)]
36. De La Beaujardiere, O.; Jeong, L.; Basu, B.; Basu, S.; Beach, T.; Bernhardt, P.; Burke, W.; Groves, K.; Heelis, R.; Holzworth, R.; et al. C/NOFS: A mission to forecast scintillations. *J. Atmos. Sol. Terr. Phys.* **2004**, *66*, 1573–1591. [[CrossRef](#)]
37. Russell, J.M.; Mlynczak, M.G., III; Gordley, L.L.; Tansock, J.; Esplin, R. An overview of the SABER experiment and preliminary calibration results. In Proceedings of the SPIE, 44th Annual Meeting, Denver, CO, USA, 18–23 July 1999; Volume 3756, pp. 277–288.
38. John, S.R.; Kumar, K.K. TIMED/SABER observations of global gravity wave climatology and their interannual variability from stratosphere to mesosphere lower thermosphere. *Clim. Dyn.* **2012**, *39*, 1489–1505. [[CrossRef](#)]
39. Mertens, C.J.; Mlynczak, M.G.; Lo’pez-Puertas, M.; Wintersteiner, P.P.; Picard, R.H.; Winick, J.R.; Gordley, L.L.; Russell, J.M., III. Retrieval of mesospheric and lower thermospheric kinetic temperature from measurements of CO₂ 15 mm Earth limb emission under non-LTE conditions. *Geophys. Res. Lett.* **2001**, *28*, 1391–1394. [[CrossRef](#)]
40. Kishore Kumar, G.; Venkat Ratnam, M.; Patra, A.K.; Vijaya Bhaskara Rao, S.; Russell, J. Mean thermal structure of the low-latitude middle atmosphere studied using Gadanki Rayleigh lidar, Rocket, and SABER/TIMED observations. *J. Geophys. Res.* **2008**, *113*, D23106. [[CrossRef](#)]
41. Ramesh, K.; Sridharan, S. Large mesospheric inversion layer due to breaking of small scale gravity waves: Evidence from Rayleigh lidar observations over Gadanki (13.51° N, 79.21° E). *J. Atmos. Sol. Terr. Phys.* **2012**, *89*, 90–97. [[CrossRef](#)]
42. Wang, L.; Geller, M.A.; Alexander, M.J. Spatial and Temporal Variations of Gravity Wave Parameters. Part I: Intrinsic Frequency, Wavelength, and Vertical Propagation Direction. *J. Atmos. Sci.* **2005**, *62*, 125–142. [[CrossRef](#)]
43. Hirota, I. Climatology of gravity waves in the middle atmosphere. *J. Atmos. Terr. Phys.* **1984**, *46*, 767–773. [[CrossRef](#)]
44. Hirota, I.; Niki, T. A statistical study of inertia-gravity waves in the middle atmosphere. *J. Meteorol. Soc.* **1985**, *63*, 1055–1066. [[CrossRef](#)]
45. Hamilton, K. Climatological Statistics of Stratospheric Inertia-Gravity Waves Deduced from Historical Rocketsonde Wind and Temperature Data. *J. Geophys. Res.* **1991**, *96*, 20831–20839. [[CrossRef](#)]
46. Eckermann, S.D.; Hirota, I.; Hocking, W.K. Gravity wave and equatorial wave morphology of the stratosphere derived from long-term rocket soundings. *Q. J. R. Meteorol. Soc.* **1994**, *121*, 149–186. [[CrossRef](#)]
47. Wang, L.; Alexander, M.J. Global estimates of gravity wave parameters from GPS radio occultation temperature data. *J. Geophys. Res.* **2010**, *115*, D21122. [[CrossRef](#)]
48. Ern, M.; Preusse, P.; Alexander, M.J.; Warner, C.D. Absolute values of gravity wave momentum flux derived from satellite data. *J. Geophys. Res.* **2004**, *109*, D20103. [[CrossRef](#)]
49. Tsuda, T.; Kato, S.; Yokoi, T.; Inoue, T.; Yamamoto, M.; Van Zandt, T.E.; Fukao, S.; Sato, T. Gravity waves in the mesosphere observed with the middle and upper atmosphere radar. *Radio Sci.* **1990**, *26*, 1005–1018. [[CrossRef](#)]
50. Tsuda, T.; Nishida, M.; Rocken, C.; Ware, R.H. A Global Morphology of Gravity Wave Activity in the Stratosphere Revealed by the GPS Occultation Data. *J. Geophys. Res.* **2000**, *105*, 7257–7273. [[CrossRef](#)]

51. Hindley, N.P.; Wright, C.J.; Smith, N.D.; Mitchell, N.J. The southern stratospheric gravity wave hot spot: Individual waves and their momentum fluxes measured by COSM GPS RO. *Atmos. Chem. Phys.* **2015**, *15*, 7797–7818. [[CrossRef](#)]
52. Faber, A.; Llamedo, P.; Schmidt, T.; de la Torre, A.; Wickert, J. On the determination of gravity wave momentum flux from GPS radio occultation data. *Atmos. Meas. Tech.* **2013**, *6*, 3169–3180. [[CrossRef](#)]
53. Bretherton, F.P. Momentum transport by gravity waves. *Q. J. R. Met. Soc.* **1969**, *95*, 213–243. [[CrossRef](#)]
54. Fritts, D.C. A review of gravity wave saturation processes effects and variability in the middle atmosphere. *Pageoph* **1989**, *130*, 343–371. [[CrossRef](#)]
55. Dunkerton, T.J. Theory of internal gravity wave saturation. *Pageoph* **1989**, *130*, 2–3. [[CrossRef](#)]
56. Fritts, D.C.; Tsuda, T.; Kato, S.; Sato, T.; Fukao, S. Observational evidence of a saturated gravity wave spectrum in the troposphere and lower stratosphere. *J. Atmos. Sci.* **1988**, *45*, 12. [[CrossRef](#)]
57. De La Torre, A.; Alexander, P.; Giraldez, A. High-resolution temperature profiles measured with stratospheric balloons near the Andes Mountains. *Geophys. Res. Lett.* **1997**, *24*, 1079–1082. [[CrossRef](#)]
58. Nastrom, G.D.; Van Zandt, T.E.; Warnock, J.M. Vertical wave-number spectra of wind and temperature from high-resolution balloon soundings over Illinois. *J. Geophys. Res.* **1997**, *102*, 6685–6701. [[CrossRef](#)]
59. Dewan, E.M.; Grossbard, N. Power spectral artifacts in published balloon data and implications regarding saturated gravity wave theories. *J. Geophys. Res.* **2000**, *105*, 4667–4683. [[CrossRef](#)]
60. Torrence, C.; Compo, G.P. A practical Guide to wavelet analysis. *Bull. Am. Meteorol. Soc.* **1998**, *79*, 1. [[CrossRef](#)]
61. Ern, M.; Preusse, P.; Gille, J.C.; Hepplewhite, C.L.; Mlynczak, M.G.; Russell, J.M., III; Riese, M. Implications for atmospheric dynamics derived from global observations of gravity wave momentum flux in stratosphere and mesosphere. *J. Geophys. Res.* **2011**, *116*, D19107. [[CrossRef](#)]
62. Djuth, F.; Sulzer, M.P.; Gonzales, S.A.; Mathews, J.D.; Elder, J.H.; Walterscheid, R.L. A continuum of gravity waves in the Arecibo thermosphere? *Geophys. Res. Lett.* **2004**, *31*, L16801. [[CrossRef](#)]
63. Oliver, W.L.; Otsuka, Y.; Sato, M.; Takami, T.; Fukao, S. A climatology of F region gravity wave propagation over the middle and upper atmosphere radar. *J. Geophys. Res.* **1997**, *102*, 14499–14512. [[CrossRef](#)]
64. Preusse, P.; Dörnbrack, A.; Eckermann, S.D.; Riese, M.; Schaeler, B.; Bacmeister, J.T.; Broutman, D.; Grossmann, K.U. Space-based measurements of stratospheric mountain waves by CRISTA 1. Sensitivity, analysis method, and a case study. *J. Geophys. Res.* **2002**, *107*, 8178. [[CrossRef](#)]
65. Tsuda, T.; Vanzandt, T.E.; Mizumoto, M.; Kato, S.; Fukao, S. Spectral Analysis of Temperature and Brunt-Väisälä Frequency Fluctuations Observed by Radiosondes. *J. Geophys. Res.* **1991**, *96*, 17265–17278. [[CrossRef](#)]
66. Vadas, S.L.; Liu, H.-L.; Lieberman, R.S. Numerical modeling of the global changes to the thermosphere and ionosphere from the dissipation of gravity waves from deep convection. *J. Geophys. Res. Space Phys.* **2014**, *119*, 7762–7793. [[CrossRef](#)]
67. Dewan, E. Saturated-cascade similitude theory of gravity wave spectra. *J. Geophys. Res.* **1997**, *102*, 799–817. [[CrossRef](#)]
68. Liu, H.; Lu, H.; Watanabe, S. A solar terminator wave in thermospheric wind and density simultaneously observed by CHAMP. *J. Geophys. Res.* **2009**, *36*, L10109. [[CrossRef](#)]
69. Djuth, F.T.; Zhang, L.D.; Livneh, D.J.; Seker, I.; Smith, S.M.; Sulzer, M.P.; Mathews, J.D.; Walterscheid, R.L. Arecibo’s thermospheric gravity waves and the case for an ocean source. *J. Geophys. Res.* **2010**, *115*, A08305. [[CrossRef](#)]
70. Fritts, D.C.; Vadas, S. Gravity wave penetration into the thermosphere: Sensitivity to solar cycle variations and mean winds. *Ann. Geophys.* **2008**, *26*, 3841–3861. [[CrossRef](#)]
71. Takahashi, H.; Taylor, M.J.; Pautet, P.-D.; Medeiros, A.F.; Gobbi, D.; Wrasse, C.M.; Fehine, J.; Abdu, M.A.; Batista, I.S.; Paula, E.; et al. Simultaneous observation of ionospheric plasma bubbles and mesospheric gravity waves during the SpreadFEX Campaign. *Ann. Geophys.* **2009**, *27*, 1477–1487. [[CrossRef](#)]
72. Vadas, S.L. Horizontal and vertical propagation and dissipation of gravity waves in the thermosphere from lower atmospheric and thermospheric sources. *J. Geophys. Res.* **2007**, *112*, A06305. [[CrossRef](#)]
73. Vadas, S.L.; Liu, H.L. Numerical modeling of the large-scale neutral and plasma responses to the body forces created by the dissipation of gravity waves from 6 h of deep convection in Brazil. *J. Geophys. Res.* **2013**, *118*, 2593–2617. [[CrossRef](#)]
74. Singh, S.; Johnson, F.S.; Powe, R.A. Gravity wave seeding of equatorial plasma bubbles. *J. Geophys. Res.* **1997**, *102*, 7399–7410. [[CrossRef](#)]
75. Kelley, M.C. *The Earth’s Ionosphere: Plasma Physics and Electrodynamics*, 2nd ed.; Academic Press: Cambridge, MA, USA, 2009.
76. Tsuda, T.; Shepherd, M.; Gopalswamy, N. Advancing the understanding of the Sun–Earth interaction—The Climate and Weather of the Sun–Earth System (CAWSES) II. *Program Earth Planet. Sci.* **2015**, *2*, 28. [[CrossRef](#)]
77. Krall, J.; Huba, J.D.; Fritts, D.C. On the seeding of equatorial spread F by gravity waves. *Geophys. Res. Lett.* **2013**, *40*, 661–664. [[CrossRef](#)]